ELSEVIER

Contents lists available at ScienceDirect

International Journal of Solids and Structures

journal homepage: www.elsevier.com/locate/ijsolstr





Examining the micromechanics of cementitious composites using *In-Situ* X-ray measurements

Ryan C. Hurley b,a,*, Darren C. Pagan c, Eric B. Herbold d, Chongpu Zhai b

- ^a Department of Mechanical Engineering, Johns Hopkins University, Baltimore, MD 21218, USA
- b Hopkins Extreme Materials Institute, Johns Hopkins University, Baltimore, MD 21218, USA
- ^c Department of Materials Science and Engineering, Pennsylvania State University, University Park, PA 16082, USA
- ^d Atmospheric, Earth, and Energy Sciences, Lawrence Livermore National Laboratory, Livermore, CA 94550, USA

ARTICLE INFO

Keywords: Cementitious composites Concrete Micromechanics theories X-ray tomography X-ray diffraction

ABSTRACT

Micromechanics theories such as Mori–Tanaka's approximation and Herve-Zaoui's layered-inclusion approximation have been used extensively to predict homogenized stiffness, inclusion stresses, and matrix strains in various composites. While these theories accurately predict homogenized properties, the accuracy of their predictions of stresses and strains within individual phases of cementitious composites has not been assessed with experimental measurements or used to infer phase properties. Here, we therefore use *in-situ* X-ray tomography, 3D X-ray diffraction, and digital volume correlation to evaluate homogenized stiffness, inclusion stresses, and matrix strains in two cementitious composites. We compare measurements with predictions of Mori–Tanaka's mean-field approximation and Herve-Zaoui's layered-inclusion approximation. We provide some of the first direct support that these micromechanics theories can accurately predict both homogenized sample stiffness and individual phase responses. We also show that combining *in-situ* X-ray measurements with these theories provides a novel route for inferring the properties of specific phases.

1. Introduction

Continuum micromechanics has been employed extensively to predict the homogenized properties of cementitious composites. Multiphase models of Hashin (1991), Mori and Tanaka (1973), Eshelby (1957), and Tanaka (1972) have been used to derive the effective elastic stiffness of cement and concrete from the volume fractions and moduli of individual phases (Ramesh et al., 1998; Yang and Huang, 1996a,b; Ulm et al., 2004; Sorelli et al., 2008). More recently, the Mori-Tanaka scheme (Li and Wang, 2008; Nemat-Nasser and Hori, 2013; Benveniste, 1987) has been used to develop a multi-scale framework for predicting the elastic and inelastic responses of cementitious composites (Königsberger et al., 2014a,b, 2018; Pichler and Hellmich, 2011). In this context, Pichler and Hellmich employed the Mori-Tanaka scheme to first upscale the properties of nanoscale phases (hydrate foam) to the microscale, and then to upscale microscale properties to the sample scale (Pichler and Hellmich, 2011). Subsequent work by these authors and others employed similar Mori-Tanaka-based transitions to predict stress and strain fields around aggregates (Königsberger et al., 2014a), the onset of failure at inclusion-matrix interfaces (the interfacial transition zone (ITZ)) (Königsberger et al., 2014b; Mihai and Jefferson, 2011), failure at hydrate-paste interfaces (Königsberger

et al., 2018), and to further estimate homogenized properties using random homogenization theory (Königsberger et al., 2020). Other models, such as Herve and Zaoui's layered-inclusion approximation (Herve and Zaoui, 1993; Christensen and Lo, 1979), rigorously capture the behavior of layered inclusions such as aggregates surrounded by ITZ and have also been used to predict elastic properties of cementitious composites (Ramesh et al., 1996; Sun et al., 2007).

The first condition required for applicability of micromechanics models is that a sufficiently large, "representative" volume of microstructure is sampled by the specimen – i.e., that the sample is large enough to be considered a representative volume element (RVE) (Drugan and Willis, 1996). By the analysis of Drugan and Willis (1996), the RVE size required to obtain 5% error in effective modulus is only twice the diameter of inclusions for any inclusion packing density in a broad class of composites. This RVE size is significantly smaller than the samples typically studied with micromechanics models, even in this paper in which miniature cementitious composite samples are examined. Other conditions related to the applicability of Mori–Tanaka models have often been challenged in the literature, despite the accurate homogenized stiffness predictions of the models (see discussion in Königsberger et al. (2018)). For instance, the applicability of Mori–Tanaka's

^{*} Corresponding author at: Department of Mechanical Engineering, Johns Hopkins University, Baltimore, MD 21218, USA. E-mail address: rhurley6@jhu.edu (R.C. Hurley).

model to some cementitious composites has been challenged because of the large volume fractions and non-elliptical shapes of inclusions in a typical cement or concrete (Königsberger et al., 2018). In the context of such challenges. A critical evaluation of Mori-Tanaka's approximation, the differential scheme, and Herve-Zaoui's approximation (called the generalized self-consistent method) has been undertaken (Christensen, 1990), with only Herve-Zaoui's approximation providing a close fit to diverse experimental data and showing reasonable behavior in high inclusion concentration limit cases. While large inclusion volume fractions may challenge the underlying assumption of a mean-field inherent to Mori-Tanaka's approximation (Li and Wang, 2008; Ferrari, 1991), motivating more advanced schemes (Nemat-Nasser and Hori, 2013), ample empirical evidence supports Mori-Tanaka's accuracy for large inclusion volume fractions realizable in cementitious composites (Klusemann et al., 2012; Königsberger et al., 2018; Sevostianov and Kachanov, 2014). Furthermore, while non-elliptical inclusion shapes violate the elliptical shape requirement of Eshelby inclusion theories (Li and Wang, 2008), Mori-Tanaka's approximation has been shown to remain accurate for such cases (Klusemann et al., 2012; Königsberger et al., 2018; Sevostianov and Kachanov, 2014).

Despite their macroscale accuracy for cementitious composites, direct experimental validation of the microscale assumptions underlying Mori-Tanaka and Herve-Zaoui approximations in these materials has been scarce. In this paper, we address three important questions related to Mori-Tanaka's mean field theory for cementitious composites: (1) do Mori-Tanaka's and Herve-Zaoui's approximations provide accurate predictions of homogenized sample stiffness? (2) do average inclusion stresses and matrix strains match those predicted by concentration operations used in Mori-Tanaka's theory in cementitious composites? (3) can discrepancies between theory and measurement be used to infer material damage? The prevailing challenge in addressing these questions has been experimental limitations which make characterization of matrix strain and inclusion stress fields difficult. X-ray tomography and digital volume correlation for cementitious composites has only recently become common and developed to the extent that qualitative and possibly quantitative comparisons with theory are possible (Hild et al., 2013; Mao et al., 2019; Stamati et al., 2019; Loeffler et al., 2018). Furthermore, in-situ measurements of stresses within crystalline inclusions surrounded by a composite matrix have been inaccessible until recent developments in 3D X-ray diffraction (3DXRD) (Oddershede et al., 2010; Poulsen, 2004; Bernier et al., 2011). The first measurements of stresses within large crystalline aggregates similar to those typically found in granular materials and cement have only been made in the past few years (Hurley et al., 2016; Hurley and Pagan, 2019; Nair et al., 2019)

In this paper, we discuss the three questions raised in the previous paragraph and address the first two using data obtained from two uniaxial stress experiments performed on small samples of cementitious composites. In the uniaxial stress experiments, we combine in-situ X-ray computed tomography (XRCT) and 3D X-ray diffraction (3DXRD) measurements, along with digital volume correlation (DVC) calculations, to examine inclusion stresses, cement paste strains, and homogenized sample stiffness. In contrast to our prior work (Hurley and Pagan, 2019) which compared only average inclusion stresses to Mori-Tanaka predictions, here we also examine average matrix strains, sample stiffness, and both Mori-Tanaka's and Herve-Zaoui's approximation to investigate which of the assumptions underlying these approximations are accurate or inaccurate, and to exploit inaccuracies to infer material properties or damage. We show that stiffness predictions made using Mori-Tanaka's and Herve-Zaoui's approximation are accurate at the macroscale for one of our samples and inaccurate for the other. Despite the inaccuracy of the stiffness prediction for the second sample, average inclusion stress calculations are very accurate for both samples. This finding and measurements of inaccurate matrix strain predictions for the same sample featuring inaccurate sample stiffness predictions leads us to conclude that the deviation from theory likely

arises from drying-induced micro-cracking or the use of elastic rather than visco-elasto-viscoplastic moduli more representative of dissipative processes occurring during stress–strain protocols. We use a simple scalar damage model to capture the effects of drying-induced micro-cracking and other dissipative processes. This work is intended to be a first step toward experimentally evaluating the applicability of continuum micromechanics and their underlying assumptions in cementitious composites. We therefore also provide a discussion of intended future work examining additional open problems.

The remainder of the paper is organized as follows. Section 2 describes the experiments, XRCT and 3DXRD measurements, and DVC calculations. Section 3 summarizes the main assumptions and equations underlying Mori–Tanaka's and Herve-Zaoui's approximations and discusses comparisons between experimental measurements and theory. Section 4 provides a discussion of results and proposed future work. Section 5 provides concluding remarks and a summary.

2. Experiment and data processing

This section describes the experiments and experimental data processing used for comparisons between micromechanics theories and measurements made in Section 3.

2.1. Sample preparation

Two cementitious composite samples made primarily from Portland cement and single-crystal quartz inclusions are described in this paper. Samples were prepared as follows and as previously described in Hurley and Pagan (2019). Single-crystal blocks (Sawyer Technical Materials, LLC) were first fragmented and ball-milled using a stainless-steel ball mill and stainless-steel vial (SPEX SamplePrep Mixer/Mill 8000D ball mill) for 30 s at room temperature. No processing control agents were used during ball milling. The resulting quartz particles were sieved to retain those between mesh numbers 60 and 80 (177 - 250 µm). Quartz particles were then combined with Type I Portland cement (Quikrete Type I/II, ASTM C150 compliant) in a 1:2 weight ratio. Water was then added until a 1:3 water to solid weight ratio was reached, for an initial water-to-cement ratio of approximately 0.5 by weight (not including the quartz particles in the weight calculation of the cement). The resulting mixture formed a slurry that flowed sufficiently well for the purpose of sample preparation. The slurry was poured into 1 cm³ cubic silicone molds. The molds were vibrated for 30 s at about 200 Hz before being covered by a thin polyethylene sheet for 24 h. After 24 h, the 1 cm³ cubes were removed from the silicone molds and submerged in a hydrated lime solution for 28 days. The hydrated lime solution consisted of tap water mixed with lime (Type S masons hydrated lime from Carmeuse, Rockwell Corporation). Finally, after 28 days the concrete cubes were removed from the hydrated lime solution and cut with a diamond-tip blade into approximately 1 mm³ cubes. The precise dimension of Sample 1 was $1.01 \times 1.03 \times 0.85$ mm and the precise dimension of Sample 2 was $1.03 \times 0.95 \times 1.0$ mm; these dimensions were determined after experiments were performed by inspecting the XRCT images. We note that controlling water to solids ratios was challenging for the size of samples prepared in this work. All ratios should therefore be assumed as approximate.

The first sample, referred to as Sample 1, was kept at room temperature for five months after cutting and prior to being studied at the Cornell High Energy Synchrotron Source (CHESS) beamline F2 as previously described in Hurley and Pagan (2019). Although our prior work described Sample 1 and some of its mechanical response, the current paper describes the application of DVC to the sample and a more thorough study of its micromechanics for the first time. The second sample, referred to as Sample 2, was kept at room temperature for approximately 12 months longer than the first sample. Sample 2 was studied at the Advanced Photon Source (APS) beamline ID-1-E. The experimental protocols for each sample are described in Section 2.2. Additional details regarding image processing and resulting phase fractions of each sample are provided in Section 2.3.

2.2. Experimental procedure and macroscopic sample response

The experimental procedure for Sample 1 was described in Hurley and Pagan (2019) and is briefly summarized here. Sample 1, which measured 1.01×1.03×0.85 mm, was compressed in a state of unconfined uniaxial stress between 1.5 mm diameter stainless-steel platens in the Rotation and Axial Motion System (RAMS) (Shade et al., 2015) load frame at CHESS beamline F2. The sample was placed within a 1.5 mm inner-diameter, 1 mm wall-thickness aluminum cylinder to capture any fragments generated during compression, but the sides of the sample remained traction-free throughout the experiment. While the interface between the stainless-steel platens and sample may have featured friction for Samples 1 and 2, the effects of this friction were ignored in the present work. An assumption of negligible friction is supported by our modeling work with Sample 1 (Wei et al., 2020), which showed that prescribing displacement boundary conditions to the top and bottom of the sample, while allowing free lateral motion, yielded a close comparison between experimental and simulated stiffness, aggregate stress, and fracture patterns with experimental observations. We note, however, that friction may not be fully absent and may enhance both the uniaxial compressive strength and stress variance throughout our samples, as suggested by prior work (Fischer et al., 2014).

Sample 1 was compressed by displacement-controlled downward motion of the stainless-steel platen touching its top surface. Displacement was imposed at approximately 0.1 µm/s, yielding a strain rate of approximately 10⁻⁴/s. At user-selected increments of macroscopic sample strain chosen to coincide with a desired macroscopic stress, the displacement of both platens were held constant and the sample was rotated 180° and then 360° while illuminated with a 41.991 keV X-ray box-beam 1.2 mm tall by 2.5 mm wide. During the first rotation, 1800 transmission radiographs were obtained at each 0.1° for X-ray computed tomography (XRCT) reconstruction. During the second rotation, 1440 diffraction patterns were obtained on far-field Dexela detectors located about 860 mm from the sample for 3D Xray diffraction (3DXRD) analysis. After both rotations, the sample was further strained prior to the next set of measurements. Throughout the experiment, the force applied to the sample was measured by a load cell with a range of 1000 N and a nonlinearity of 5 N.

Sample 2, which measured $1.03 \times 0.95 \times 1.0$ mm, was also subjected to uniaxial stress between two 1.5 mm diameter stainless-steel platens. The sample was also placed in a 1.5 mm inner-diameter, 1 mm wall-thickness aluminum cylinder to capture any fragments generated during compression, but its sides remained traction-free throughout the experiment. The experiment performed on Sample 2 used a custombuilt load frame shown in Fig. 1(a) and described in Zhai et al. (2020). The load frame features a linear actuator with encoder (Haydon Kerk Size 34 Stepper Motor) and load cell (Futek LCM200 with a range of 2224 N and a nonlinearity of 11.1 N) to compress samples to a desired load level between stainless-steel platens. The load frame was designed to permit ultrasound transmission measurements during compression, as described in Zhai et al. (2020), and is operated fully within a National Instruments (NI) Labview environment. The sample was also compressed by displacement-controlled downward motion of the stainless-steel platen touching its top surface. Displacement was again imposed at approximately 0.1 µm/s, yielding a strain rate of approximately $10^{-4}/s$. At user-selected increments of macroscopic sample strain, the displacement of the loading platen was held constant and the sample was rotated 180° and then 360° while illuminated with a 51.618 keV X-ray box-beam 1.2 mm tall by 2.0 mm wide. The same number of transmission radiographs and diffraction patterns were obtained during each rotation as for Sample 1. For Sample 2, the far-field GE detector used for X-ray diffraction analysis was located about 1200 mm from the sample. Throughout the experiment, the force applied to the sample was measured by the load cell. A schematic of the experimental setup is shown in Fig. 1(b) and provides a simpler

view of the important components of the experimental setup shown in Fig. 1(a).

The load cell readings immediately after applying a sample strain increment (labeled "(Pre)") and during 3DXRD measurements (labeled "Post") for each sample are shown in Fig. 2(b) as a function of load step. A significant amount of relaxation without sample strain was observed between the end of strain application and measurements. We attribute this relaxation to slow sliding on internal micro-cracks and defects in the samples and possible internal sliding of components within the load frames. A majority of the observed relaxation occurred during the XRCT scans at each load step, which were performed over the duration of approximately 30 min. Prior research has found infinite creep compliance upon changes in mechanical loading on concrete specimens, with a reduction to slower creep over several minutes (Irfan-ul Hassan et al., 2016), suggesting that much of the relaxation we observed likely occurred immediately after straining on our samples. No motion blur was observed in the XRCT images, which were reconstructed using radiographs obtained over a period of 30 min. The presence of obvious motion blur would suggest that the microstructure of the samples was changing significantly (at least at the scale of the pixel size) during the acquisition of radiographs at different angles. The absence of motion blur suggests that material creep was insignificant at the length scale of a of the pixel size (described in Section 2.3) in each experiment. The macroscopic stress-strain curves calculated by dividing the load cell readings during strain application (the "(Pre)" points) by initial sample cross-sectional area are shown in Fig. 2(a). The macroscopic strains were calculated by registration of XRCT images for the entire sample in the open-source Software for Practical Analysis of Materials (SPAM) (Stamati et al., 2020), which is also used for DVC and is described in Section 2.4. The macroscopic stress in Fig. 2(a) is assumed to be representative of the material state prior to relaxation and is therefore not considered a representative of a visco-elastic material response.

We note that for both Sample 1 and 2, mixed displacement–traction boundary conditions were applied, with displacements applied to the sample in the compression direction and stress-free boundary conditions applied in the other directions. The instantaneous ("Pre") and relaxed ("Post") stress measurements are both used to compare to our calculations and measurements. For instance, we compare macroscopic sample stiffness measurements with stresses calculated using load cell measurements during strain application ("Pre"). This is similar to using the steepest part of the stress–strain curve (often the initial points on the unloading curve) to compute sample stiffness. On the other hand, we compare aggregate stresses measured using 3DXRD (described in Section 2.5) with micromechanics predictions that employ the farfield stresses calculated using load cell measurements after relaxation ("Post").

2.3. X-ray computed tomography and phase segmentation

XRCT images were reconstructed for Sample 1 using the iterative ASD-POCS algorithm in Livermore Tomography Tools (LTT) (Sidky and Pan, 2008; Champley, 2016), as described in Hurley and Pagan (2019). The resulting images had a pixel size of 1.48 μm per pixel. ASD-POCS was used for Sample 1 because of the poor contrast between phase fractions that occurred when using a traditional Filtered Back-Projection (FBP) algorithm for reconstruction. XRCT images were reconstructed for Sample 2 using the FBP algorithm in TomoPy (Gürsoy et al., 2014). The resulting images had a resolution of 1.172 µm per pixel. All XRCT images were 32-bit with grey-scale values corresponding to the local X-ray attenuation coefficient calculated during reconstruction. 32-bit images were converted to 16-bit images for ease of data processing by manually selecting a minimum and maximum grey-scale value in 32-bit images and linearly scaling this range to a 16-bit range: 0 to 65,535. The same minimum and maximum grey-scale value was used for all images for each sample to ensure that a grey-scale value in one load

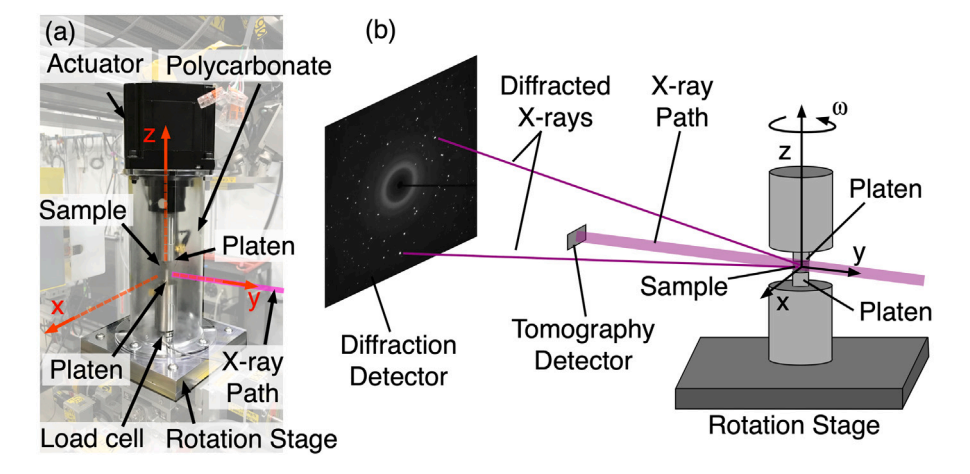


Fig. 1. (a) Sample tested at APS. (b) Schematic of experiment.

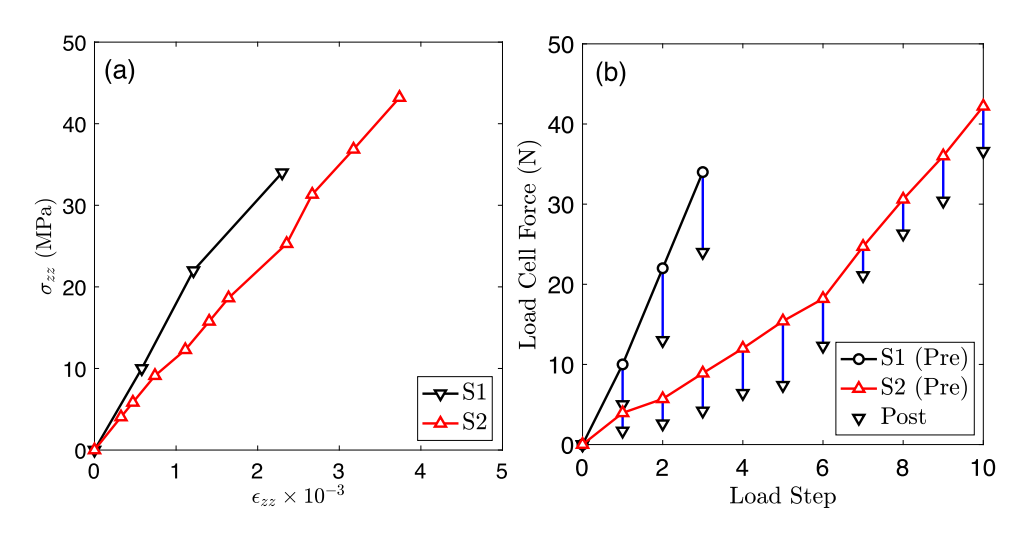


Fig. 2. (a) Stress versus strain. Stress was computed from the load cell readings after strain application ("Pre" in (a)). Strain was computed from full-sample registration of XRCT images, as described in Section 2.4. S1 refers to Sample 1 and S2 is Sample 2. (b) Load cell versus load step.

step corresponded to the same phase as a grey-scale value in another load step for that sample. We note that although the XRCT image resolution differed for Samples 1 and 2, we did not re-scale images from the two samples to feature matching resolution. Such re-scaling would introduce noise that would affect segmentation and DVC calculations.

After all XRCT images for both samples were reconstructed, image processing and phase segmentation was performed using Matlab. Phases observable by eye in all XRCT images include voids or fractures, single-crystal quartz inclusions sometimes referred to here as quartz aggregates, a low-density cement paste, and a high density cement paste phase. The XRCT images for both samples and two horizontal cross-sections are shown in Fig. 3, with each phase labeled. Variations in grey-scale intensity exist for each phase, but voids, low-density cement paste phases, and high-density cement paste phases can generally be separated by simply isolating pixels with a grey-scale value between certain ranges, as described in Hurley and Pagan (2019). Voids on the scale of several microns were more-easily segmented for Sample 2 than for Sample 1 because the reconstruction algorithm for Sample 1 effectively filtered-out features smaller than a certain length scale (see 2.4 for a discussion of feature sizes for DVC).

Quartz inclusions could only be isolated by applying a standard deviation filter to the XRCT images, as described in our prior work and by others (Hurley and Pagan, 2019; Stamati et al., 2019, 2018; Thakur et al., 2023). The standard deviation filter is only useful in isolating quartz inclusions because X-ray attenuation coefficients within

inclusions are homogeneous, in contrast to the heterogeneous attenuation coefficients found throughout the matrix. The standard deviation filter involved calculating the standard deviation of grey-scale values in $17 \times 17 \times 17$ cubic windows of pixels (erroneously defined as $18 \times 18 \times 18$ in Hurley and Pagan (2019)) of pixels around each pixel in each XRCT image (25.16 µm side-length cubic region for Sample 1 and 19.92 μm side-length cubic region for Sample 2). If the standard deviation of grey-scale values in these windows was less than 1850 for Sample 1 and less than 2000 for Sample 2, the center point of the window was labeled an inclusion pixel. 52 quartz inclusions were found in Sample 1 and 15 were found in Sample 2 using this approach. In Sample 1, quartz inclusions had an average equivalent diameter of approximately 140 µm with a standard deviation of 66 µm. In Sample 2, quartz inclusions had an average equivalent diameter of 247 µm with a standard deviation of $102~\mu m$. We note that although care was taken to fully mix quartz particles with other ingredients during the sample preparation process described in Section 2.1, the difference in inclusion sizes in Samples 1 and 2 reflects poor mixing. Nevertheless, both samples are of an appropriate size for application of homogenization schemes, as described in Section 3, and will be analyzed in the context of their respective phase fractions in subsequent sections.

After inclusion pixels were identified for each XRCT image, the pixels were dilated with a $13 \times 13 \times 13$ cubic structuring element - a size found by trial and error to give a very close visual reconstruction of the inclusion sizes and shapes. Size and shape analysis of inclusions was then performed using a connected-components algorithm in Matlab

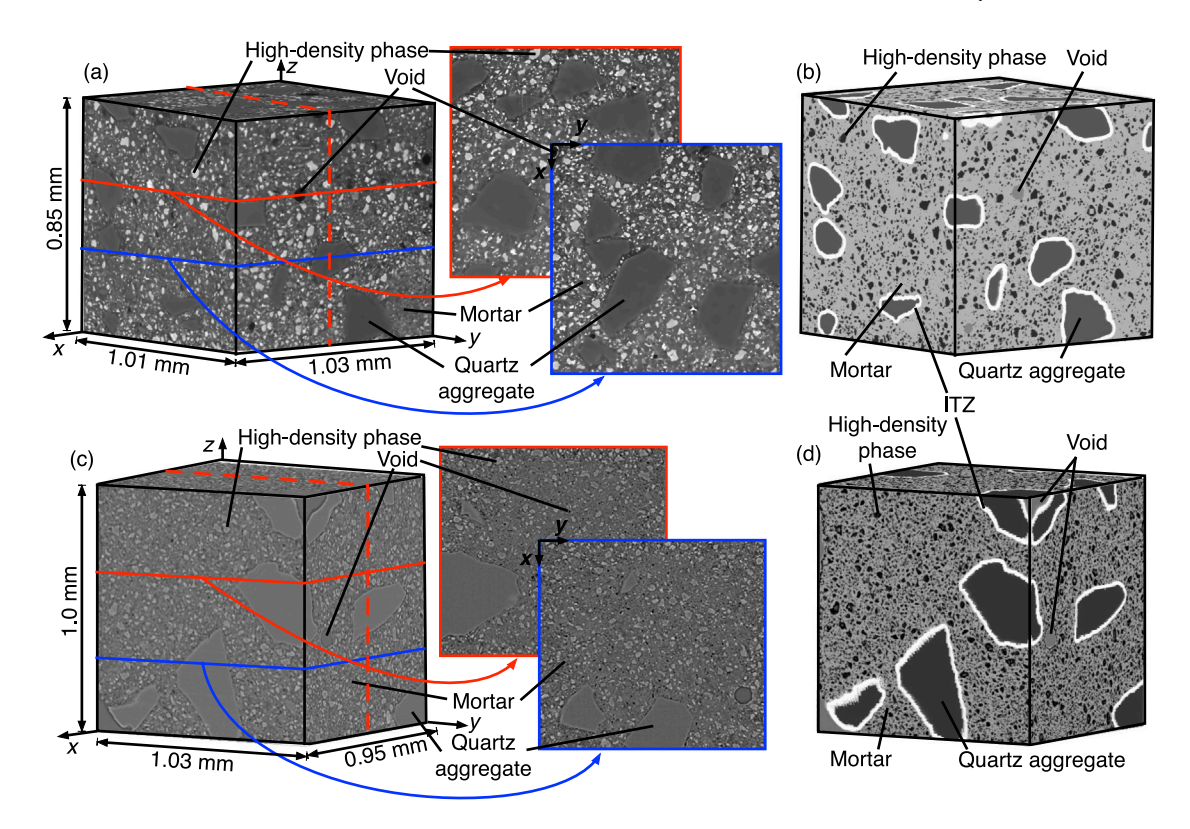


Fig. 3. (a) XRCT image of Sample 1. (b) Segmented image of the sample shown in (a) with individual phases distinguished by greyscale intensity and manually labeled. (c) XRCT image of sample 2. (d) Segmented image of the Sample shown in (c) with individual phases distinguished by greyscale intensity and manually labeled.

Table 1
Phase fractions for Samples 1 and 2. LD stands for low-density. CM stands for cement paste. HD stands for high-density.

Sample	Inclusions (f_{agg})	LD CM (f_{cp})	ITZ (f_{itz})	Void (f_v)	HD CM (f_{hd})	CM Total
1	0.18	0.56	0.10	0.01	0.15	0.71
2	0.15	0.55	0.06	0.03	0.21	0.76

that assigned pixels to a single inclusion if they were connected to one another by their face, edge, or corner (the "26-connected" structuring element). The standard deviation thresholds (1850 and 2000) were selected by trial and error: thresholds were gradually increased until segmented and dilated quartz inclusions appeared nearly identical to those discernible by eye in XRCT images. Because voids were identified as inclusion pixels by the standard deviation filter, care was taken to assemble segmented XRCT images by assigning pixels first to quartz inclusions, and then to voids, mortar, and hydration products, overwriting pixel assignments for quartz inclusions as needed. We note that XRCT images for Sample 2 featured minor phase contrast (Mayo et al., 2003), increasing grey-scale values at inclusion-mortar boundaries. All segmented XRCT images for Sample 2 were therefore post-processed to convert any pixel within 5 pixels of a quartz inclusion that was initially found to be a high-density phase into a low-density phase.

For the micromechanics calculations using the Herve-Zaoui approximation in Section 3, phase fractions of interfacial transition zones (ITZ) are also considered. ITZs could not be identified by our image analysis because they did not feature a consistent reduction in grey-scale value. For micromechanics calculations in which we consider ITZ as a separate phase from cement paste, we therefore adopt the findings of prior work suggesting that the ITZ is approximately 15 µm thick (Scrivener et al., 2004; Mondal et al., 2009). A sensitivity study of the influence of the ITZ thickness on our analysis in this paper may be performed in the future but is not expected to significantly affect our results in this paper because ITZ is assigned a stiffness equal to 85% of the cement paste. To find the phase fraction of ITZ, we therefore further dilate inclusions with spherical structuring elements with radii of 10 pixels (14.8 µm)

for Sample 1 and 13 pixels (15.2 $\mu m)$ for Sample 2. The resulting phase fractions of Samples 1 and 2 calculated using the XRCT image at load step 0 are shown in Table 1.

2.4. Digital volume correlation (DVC)

To calculate strain fields in the microstructures of each sample throughout the experiments, we performed DVC in SPAM (Stamati et al., 2020) between the initial 16-bit XRCT image for each sample and each subsequent 16-bit XRCT image. DVC in SPAM involves tessellating the 16-bit XRCT images into cubic correlation windows within which the Lucas and Kanade approach is employed in determining window displacement and rotation (Lucas and Kanade, 1981). DVC was used to calculate the strain throughout the entirety of both samples, with the exception of any regions in which correlation windows overlapped quartz inclusions or void space. Correlation windows overlapping quartz inclusions and voids were excluded from DVC analysis because such regions did not feature appropriate speckle or contrast. DVC requires a speckle pattern within each correlation window and a window size that oversamples that pattern sufficiently to avoid bias or error in displacement calculations (Sutton et al., 2009). The speckle pattern in our DVC was the natural heterogeneity present in the cement paste: the high-density phases and voids visible in Figs. 4(b) and (c). Typically, a correlation window size of 3-6 times the average feature size of the speckle pattern is suggested to ensure over-sampling (Sutton et al., 2009). To assess the average feature size for each sample, we first manually-selected 3D correlation windows from the initial XRCT image of each sample that did not contain quartz aggregates or large voids. We selected

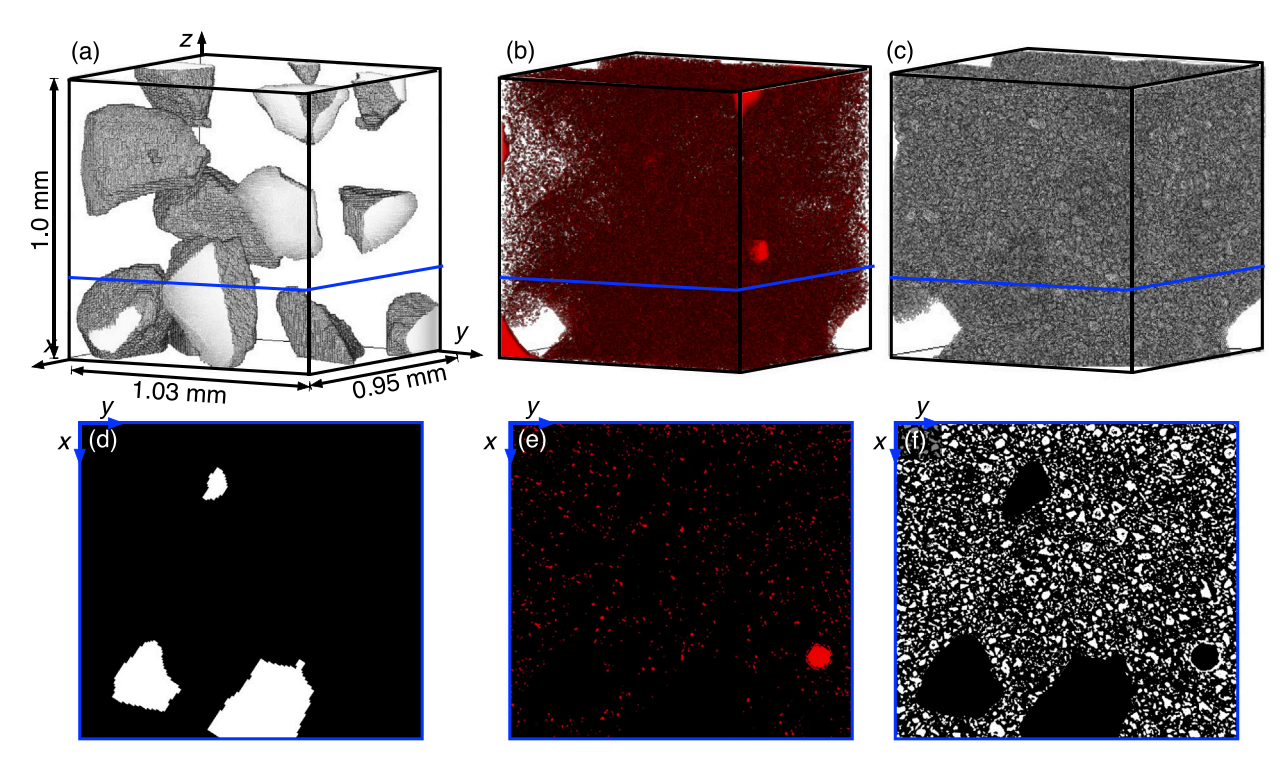


Fig. 4. (a) XRCT image of Sample 2 at load step 0 with only quartz inclusions rendered. (b) XRCT image of Sample 2 at load step 0 with only voids rendered. (c) XRCT image of Sample 2 at load step 0 with only high-density phases rendered. (d)–(e) Two-dimensional planes through (a)–(c) showing a horizontal cross-section of quartz inclusions, voids, and high-density phases, respectively, at the location of lines shown in (a)–(c). Similar figures are available for Sample 1 in Hurley and Pagan (2019).

windows of a sufficient size to ensure that our results did not depend on window size; this was verified by trial and error. We then computed the normalized autocorrelation of each correlation window. For instance, to calculate the normalized autocorrelation A of an window (or image), I, centered at coordinates (x, y, z), we calculated

$$A(i) = \frac{\sum_{i=-N}^{N} \sum_{x,y,z} I(x,y,z) : I(x-i,y,z)}{\sum_{x,y,z} I(x,y,z) : I(x,y,z)},$$
(1)

where i is an offset of the image in pixels, ranging from -N to N pixels. We performed this calculation for offsets in the x, y, and z direction. The feature size is found to be the full-width-at-half-max (FWHM) of the normalized autocorrelation function (Sutton et al., 2009).

Fig. 5(a) shows cubic regions of the XRCT images or segmented phases of the XRCT images for Samples 1 and 2. The cubic regions measure 80-pixels per side, large enough to evaluate characteristic sizes of features that can serve as speckles for DVC but small enough to prevent the regions from overlapping aggregates or large voids. These cubic regions were used only to assess feature and correlation window sizes for each sample. DVC was subsequently performed in all correlation windows tessellating the volume of the samples, with the exception of those overlapping quartz inclusions and voids. Figs. 5(b)-(f) show autocorrelation calculations obtained by translating these windows by integer pixel values and using Eq. (1). The width-at-halfmax is approximately 8 pixels in Fig. 5(b) for Sample 1 and 7 pixels in Fig. 5(d) for Sample 2, suggesting that a correlation window size of 24 - 48 pixels for Sample 1 and 21 - 42 pixels for Sample 2 is sufficiently large (Sutton et al., 2009). For simplicity, we chose a cubic correlation window of 36-pixels side length for all analysis in this paper. Figs. 5(c), (e), and (f) are provided to illustrate the feature sizes of high-density phases and voids, both of which furnish a "speckle" used by DVC algorithms.

Strain fields in the z direction (ϵ_{zz}) are shown for a select number of DVC calculations in Fig. 6 for Samples 1 and 2. The vertical sample cross-sections shown in this figure correspond to the dashed line shown in Fig. 3 on the XRCT image of each sample. Strains are

not calculated in correlation windows overlapping aggregates in XRCT images because such windows do not feature appropriate speckle for DVC; strains were therefore not rendered in aggregates. Dark colors and color variations seen at the boundary of the aggregates are an artifact of rendering a microstructure with missing data and should not be interpreted as strains. In Fig. 6, we observe an increase in compressive strain as loading of each sample progresses, with strain concentrations observed at the top and bottom of some aggregates and highlighted with blue arrows. Strains will be analyzed quantitatively in relation to micromechanics theories in Section 3. We note that visualizing strain invariants in figures analogous to Fig. 6 is also insightful for observing strain concentrations; however, we do not use these strain invariants and therefore do not render them here.

In addition to calculating strain fields using DVC, we also performed full-sample registration using DVC, treating the entire XRCT image of each sample as correlation windows and once again using the Lucas and Kanade approach in SPAM (Stamati et al., 2020). The result of these registration calculations was the sample strain at each load step. This sample strain was found to be more accurate than the strain calculated using either the encoder in the actuator or manual observation of the distance between stainless-steel platens in the XRCT images. The latter approach for calculating strain has an accuracy limited by the pixel size whereas the DVC approach has sub-pixel resolution.

2.5. 3D X-ray diffraction and grain stresses

3DXRD analysis was performed for Sample 1 using HEXRD (Bernier et al., 2011) and for Sample 2 using MIDAS (Park et al., 2015). The objective of 3DXRD for each sample was to determine the average stress tensor in each of the 52 quartz aggregates of Sample 1 and 15 quartz aggregates of Sample 2 at each load step of the experiments. For each sample, we calibrated detector orientation, tilt, and distance by using an X-ray powder diffraction pattern obtain from cerium oxide (CeO₂) immediately prior to testing our sample. Further refinements to detector orientation, tilt, and distance were also performed using the diffraction pattern obtained at load step 0 for each sample, when

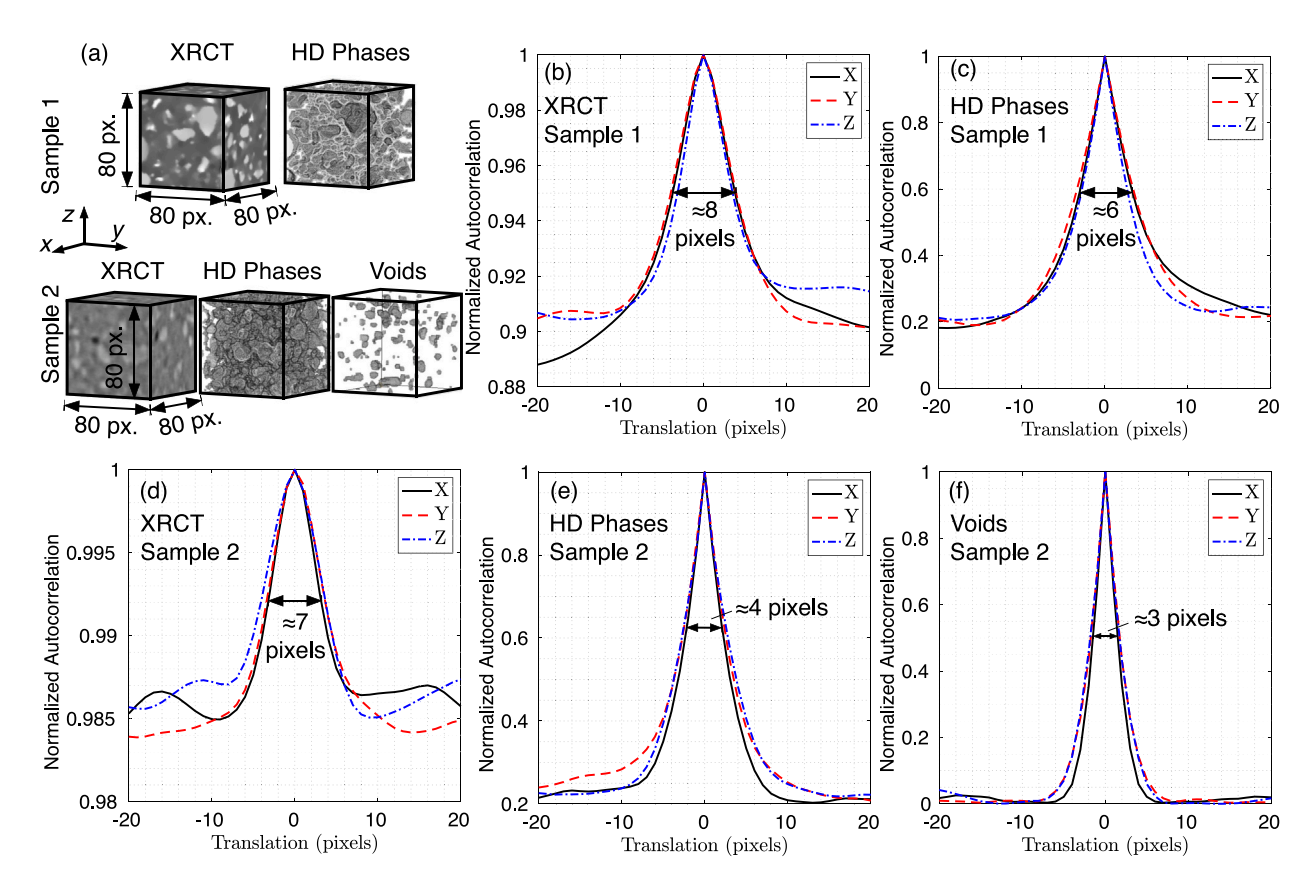


Fig. 5. (a) 80-voxel per side cubic correlation windows from XRCT images used in DVC for Sample 1 and 2 with high-density phases (HD phase) and voids isolated (the latter only for Sample 2). The correlation windows shown were isolated from the full XRCT images at load step 0 for each sample (Figs. 3(a) and (c)). (b)–(f) show the autocorrelation coefficients obtained by translating the correlation windows by integer pixels in x, y and z and using Eq. (1). The inset text conveys the sample and whether the full XRCT image was used in cross-correlation or 3D images with only the HD phases or voids rendered.

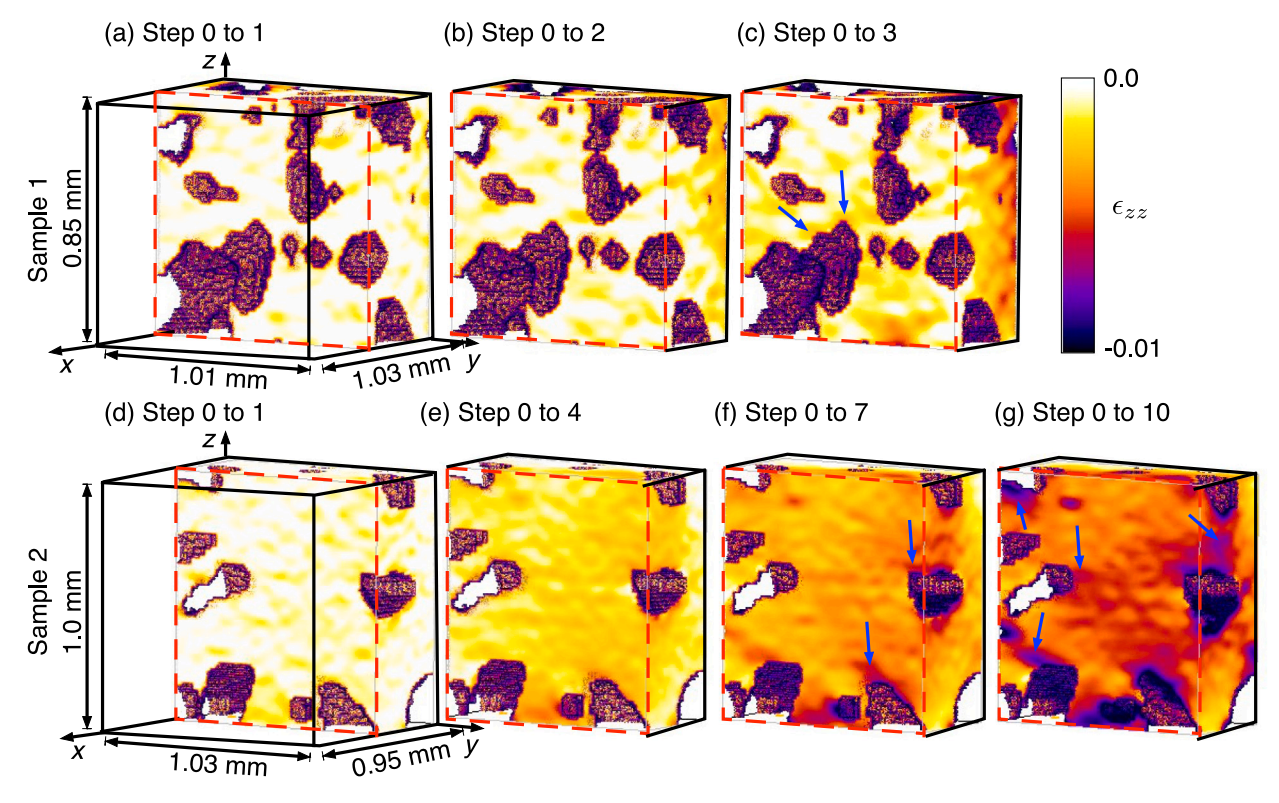


Fig. 6. Strains calculated by DVC in Sample 1 (a)–(c) between XRCT images at load steps 0 and 1 (a), 0 and 2 (b), and 0 and 3 (c). Strains calculated by DVC in Sample 2 (d)–(g) between XRCT images at load steps 0 and 1 (d), 0 and 4 (e), 0 and 7 (f) and 0 and 10 (g).

the sample was not subjected to macroscopic strain. We then applied a threshold to remove background noise from each diffraction pattern and employed the unit cell parameters of single-crystal alpha quartz (space group 154, a = 4.9411 Å, c = 5.4071 Å) to locate Bragg peaks produced by the quartz crystals. HEXRD and MIDAS performed indexing on Bragg peaks to associate them with orientations of distinct quartz particles, yielding centers-of-mass locations, quartz particle orientations, and average per-particle strain tensors \bar{e}^p , with p as a particle index, with assumed resolutions of several microns, 0.05° , and 10^{-4} per strain tensor component, respectively. We have confirmed the assumed location, orientation, and strain resolutions in prior work (Hurley et al., 2018; Hurley, 2021). Quartz particles were only assigned locations, orientations, and strains if their completeness – the ratio of number of found to predicted diffraction peaks – exceeded 0.7 in HEXRD and 0.6 in MIDAS.

The average stresses in each quartz particle were calculated from the known fourth-order stiffness tensor of alpha-quartz, $C_{11} = 87.16$ GPa, $C_{33} = 106.00$ GPa, $C_{44} = 58.14$ GPa, $C_{12} = 6.64$ GPa, $C_{13} = 12.09$ GPa, $C_{14} = -18.15$ GPa (in Voigt notation) and Hooke's law $\bar{\sigma}_{ij}^p = C_{ijkl}^{\Omega} \bar{\epsilon}_{kl}^p$, where C_{ijkl}^{Ω} is the fourth-order stiffness tensor for alpha-quartz in index notation. We note that an isotropic stiffness is assumed for quartz particles later in this paper to simplify the application of Mori-Tanaka's and Herve-Zaoui's approximations. Stresses were calculated in each particle's crystal reference frame and then transformed to the sample coordinate frame for further analysis. Particles were tracked across load steps by finding the nearest particle center-of-mass (usually within about 30 µm) in sequential load steps. When no particle center-ofmass is within 30 µm in subsequent load steps, we conclude that Bragg peaks for the particle in the load step in which it is missing could not be reliably fit by HEXRD or MIDAS. Missing a particle in a single load step may occur for a number of reasons, including fracture or if the number of Bragg peaks falls below the completeness criterion due to noise, overlap with other peaks, or particle motion after during a sample rotation (i.e., due to prior debonding of the particle from the surrounding matrix). Prior to tracking particles between load steps, Dauphine-twinned quartz particles were identified and their stresses merged as described in our previous work (Hurley et al., 2018; Hurley and Pagan, 2019).

Fig. 7(a) shows the fraction of tracked grains for Samples 1 (of 52 grains) and 2 (of 15 grains) across all load steps of each experiment. Figs. 7(b)–(c) show the evolution of volume-averaged particle stresses across all load steps. The volume-averaged particle stresses were calculated by

$$\bar{\sigma} = \frac{1}{\sum_{p=1}^{N_{XRD}^{p}} V_{p}} \sum_{p=1}^{N_{XRD}^{p}} \bar{\sigma}^{p} V_{p}$$
 (2)

where N_{XRD}^p is the number of particles for which 3DXRD measurements are available at a given load step, $\bar{\sigma}_p$ is the average stress tensor for particle p and V_p is the volume of particle p.

The stresses for Samples 1 and 2 in Fig. 7 generally follow the macroscopic load–displacement trends shown in Fig. 2. Average vertical stresses, $\bar{\sigma}_{zz}$, had the greatest magnitude, with horizontal and shear stresses having significantly lower stresses, consistent with the uniaxial stress boundary conditions. For both samples, peak volume-averaged inclusion stresses in the loading direction immediately prior to catastrophic sample stresses reached approximately -60 MPa. For Sample 2, horizontal stresses are significantly lower than those in Sample 1. Based on our findings of Section 3, we conclude that this is likely due to drying-induced in the matrix of Sample 2, which reduces the ability of the sample to transfer lateral tensile stresses to inclusions, or other dissipative processes which arise but are not properly captured by interpreting sample response through classical elastic moduli.

Fig. 8 shows 3D renderings of only the quartz inclusions for each sample, with colors representing the stress tensor component $\bar{\sigma}_{zz}^p$. The volume rendered in this figure is the same as that in Fig. 6. Inclusions

for which no matching 3DXRD measurement is available for all load steps of the experiments are highlighted in Fig. 8(a) and (e) by black arrows and given a color corresponding to $\bar{\sigma}_{zz}^p = 0$. Fig. 8 illustrates the growing compressive stress present within many of the inclusions as each experiment progresses. It also highlights the heterogeneity of inclusion stresses throughout the samples, a point that will be addressed quantitatively in analysis of a Mori–Tanaka estimates of inclusion stress.

3. Micromechanics analysis and discussion

One of the most popular homogenization schemes for estimating the homogenized properties of cementitious composites is the Mori-Tanaka approximation (Königsberger et al., 2014a; Hurley and Pagan, 2019; Yang and Huang, 1996a,b; Mihai and Jefferson, 2011). This approximation has been employed extensively to predict macroscopic moduli and to perform multiple "downscaling" calculations, whereby the effects of macroscopic stress on aggregate or hydrate interfacial failure is quantified (Königsberger et al., 2014a,b, 2018). The approximation is appropriate for a composite containing elliptical inclusions embedded in a matrix (Li and Wang, 2008; Mori and Tanaka, 1973). The introduction of this paper summarizes some of the debate surrounding the applicability of Mori-Tanaka's approximation in a medium containing a high concentration of possibly-interacting non-elliptical inclusions. Several studies support the notion that Mori-Tanaka approximations of homogenized sample stiffness are accurate, even when high concentrations of interacting inclusions are present in a matrix. Other studies have shown that the Mori-Tanaka approximation provides an accurate estimate for homogenized properties when inclusions are not elliptical and potentially concentrated at a high density within the matrix (Klusemann et al., 2012). Only one study to-date has confirmed that the aggregate stresses used within the Mori-Tanaka approximation are accurate (Hurley and Pagan, 2019), although only on average; the variance in aggregate stresses suggests significant aggregate interaction. With the addition of DVC measurements and more thorough microscale analysis in the present paper, we can also examine the accuracy of other micromechanical quantities used within the Mori-Tanaka approximation and exploit those quantities to infer material properties and damage. In particular, we examine the accuracy of average matrix strains - the "mean-field" that gives Mori-Tanaka the classification as a "mean-field theory" - and average inclusion stresses using Eshelby's single inclusion solution. Examining these quantities addresses the questions posed in the introduction to this paper and will provide insight into the microscale stress and strain heterogeneity in cementitious composites.

The Herve-Zaoui layered inclusion model has also been proposed for predicting the homogenized properties of composites containing layered inclusions, such as an aggregate inclusion surrounded by an ITZ (Ramesh et al., 1996; Sun et al., 2007). To-date, there has been favorable comparison of Herve-Zaoui's model predictions with a broad range of composites containing layered inclusions (Christensen, 1990).

In this section, we first introduce Mori–Tanaka's and Herve-Zaoui's approximations and related aspects of inclusion problems. We then compare experimental results to theoretical quantities. We note that the size of our samples, approximately 1 mm³ cubes, is assumed to be sufficiently large for the samples to be considered representative volume elements by the definition provided in Drugan and Willis (1996): both samples are more than twice the size of the largest inclusion.

3.1. Description of Mori–Tanaka's approximation for homogenized properties

We begin with a brief description of the salient components of the Mori–Tanaka approximation that have been derived elsewhere (Nemat-Nasser and Hori, 2013; Li and Wang, 2008). In the Mori–Tanaka

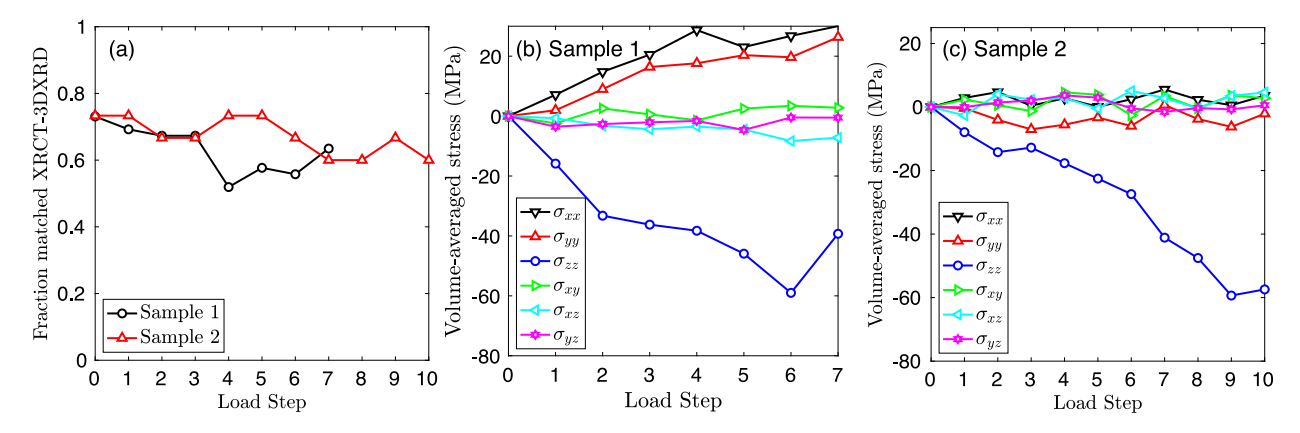


Fig. 7. (a) Fraction of inclusions observed in XRCT for which 3DXRD measurements were accurately made, as described in the main text. (b) Average stress in inclusions for Sample 1, calculated using Eq. (2). (c) Average stress in inclusions for Sample 2, calculated using Eq. (2).

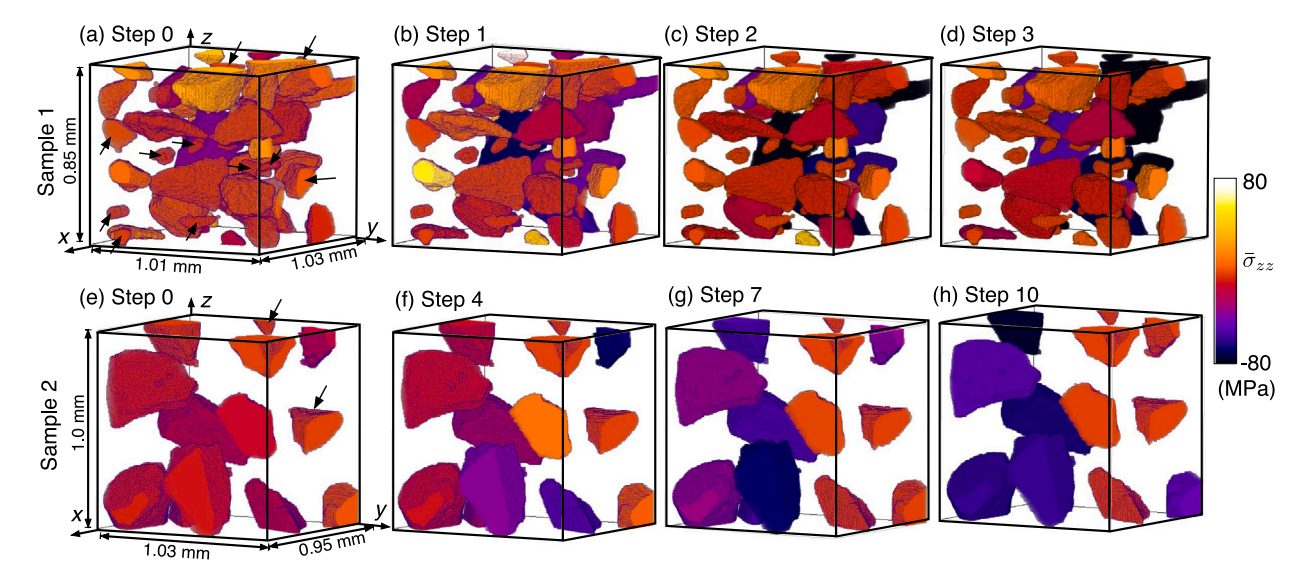


Fig. 8. Aggregate stresses for (a)–(d) Sample 1 and (e)–(h) Sample 2. Arrows in (a) and (e) highlight the visible aggregates in each sample for which no 3DXRD measurements are available throughout the entirety of the experiments. Aggregates with no 3DXRD measurements are given a color corresponding to $\bar{\sigma}_{zz}$ in each load step that 3DXRD measurements are missing. The aggregates, if visible in the subfigures, are also noted with arrows. All subfigures share the same colorbar.

approximation, a composite volume composed of a matrix and inclusions is subjected to far-field displacements or tractions, or equivalently to a far-field strain, e^{∞} , or stress, σ^{∞} . When far-field strain is applied to an infinite homogeneous medium, Mori and Tanaka showed that the integral of disturbance strains induced by the introduction of an inclusion into the matrix is zero (Tanaka, 1972). If the matrix is assumed to be the dominant phase and the introduction of an additional inclusion does not significantly alter the phase fraction of the matrix and inclusion, one can then assume $\bar{\epsilon}_M = \epsilon^\infty$. Equivalently, one can also assume $\bar{\sigma}_M = \sigma^{\infty}$ (Nemat-Nasser and Hori, 2013; Li and Wang, 2008). This is the critical assumption of Mori–Tanaka's approximation: that there is a mean-field stress or strain surrounding inclusions with properties of the matrix. This assumption makes calculations tractable but is often a point of criticism (e.g., Königsberger et al. (2018)) and differentiates Mori-Tanaka approximations from differential schemes and others in which incremental additions of inclusions do in fact alter the strains, stresses, and compliances of the effective medium in which inclusions are embedded (Nemat-Nasser and Hori, 2013; Zaoui, 2002; Pichler and Dormieux, 2008).

When far-field strains are applied to the composite, average matrix strain can be related to the average inclusion strain through

$$\bar{\epsilon}_{\Omega} = \mathbb{A}_{\Omega} : (\mathbb{A}_{\Omega} - \mathbb{S}_{\Omega})^{-1} : \bar{\epsilon}_{M}, \tag{3}$$

where $\mathbb{A}_{\varOmega}=(\mathbb{C}_{M}-\mathbb{C}_{\varOmega})^{-1}:\mathbb{C}_{M}$ is a stiffness misfit tensor of the inclusion of phase \varOmega , with \mathbb{C}_{M} the matrix stiffness tensor and \mathbb{C}_{\varOmega} the stiffness tensor of phase \varOmega , and \mathbb{S}_{\varOmega} is the infinite-domain Eshelby tensor for the inclusion of phase \varOmega . The quantity $\mathcal{A}_{\varOmega}=\mathbb{A}_{\varOmega}:(\mathbb{A}_{\varOmega}-\mathbb{S}_{\varOmega})^{-1}$ is also called the strain concentration tensor. For spherical inclusions, \mathbb{S}_{\varOmega} is given by (in index notation, with the subscript \varOmega written as a superscript) (Nemat-Nasser and Hori, 2013; Li and Wang, 2008)

$$\mathbb{S}_{ijkl}^{\Omega} = \frac{5\nu - 1}{15(1 - \nu)} \delta_{ij} \delta_{kl} + \frac{(4 - 5\nu)}{15(1 - \nu)} (\delta_{ik} \delta_{jl} + \delta_{jk} \delta_{il}), \tag{4}$$

where ν is the Poisson's ratio of the matrix phase. Similarly, when farfield stresses are applied to the composite, inclusion stresses are given by (Benveniste, 1987; Li and Wang, 2008)

$$\bar{\sigma}_{\Omega} = \mathbb{B}_{\Omega} : (\mathbb{B}_{\Omega} - \mathbb{T}_{\Omega})^{-1} : \bar{\sigma}_{M},$$
 (5)

where $\mathbb{B}_{\varOmega}=(\mathbb{D}_{M}-\mathbb{D}_{\varOmega})^{-1}:\mathbb{D}_{M}$ is a compliance misfit tensor of the inclusion phase \varOmega , with \mathbb{D}_{M} the matrix compliance tensor and \mathbb{D}_{\varOmega} the compliance tensor of phase \varOmega . The quantity $\mathcal{B}_{\varOmega}=\mathbb{B}_{\varOmega}:(\mathbb{B}_{\varOmega}-\mathbb{T}_{\varOmega})^{-1}$ is also called the stress concentration tensor. \mathbb{T}_{\varOmega} is the conjugate Eshelby tensor defined through the relation

$$\mathbb{T}_{\Omega} = \mathbb{I}^{(4s)} - \mathbb{C}_{M} : \mathbb{S}_{\Omega} : \mathbb{D}_{M}. \tag{6}$$

When far-field stresses are applied to the composite, one can also relate average matrix strain to far-field stress simply by

$$\bar{\epsilon}_M = \mathbb{C}_M^{-1} : \bar{\sigma}_M = \mathbb{C}_M^{-1} : \bar{\sigma}^{\infty}. \tag{7}$$

It has been shown that using the infinite-domain Eshelby tensors for spherical inclusions yields comparable results to using more accurate tensors for elliptical inclusions (Klusemann et al., 2012). We note that there are no length scales in Eq. (5) that would make $\bar{\sigma}_{\Omega}$ vary as a function of inclusion size. Thus, even if individual inclusions are represented by the index Ω , inclusion stresses only vary if \mathbb{S}_{Ω} or \mathbb{C}_{Ω} vary.

Using the volumetric decomposition of average composite stress or strain, where f is the inclusion phase volume fraction,

$$\bar{e} = (1 - f)\bar{e}_M + f\bar{e}_\Omega$$
 and
$$\bar{\sigma} = (1 - f)\bar{\sigma}_M + f\bar{\sigma}_\Omega,$$
 (8)

the relations $\bar{\sigma}_M=\mathbb{C}_M$: $\bar{\epsilon}_M$ and $\bar{\sigma}_\varOmega=\mathbb{C}_\varOmega$: $\bar{\epsilon}_\varOmega$, and Eqs. (3) and (5), we arrive at two expressions for the composite stress, $\bar{\sigma}$. These two expressions are

$$\bar{\sigma} = ((1 - f)\mathbb{C}_M + f\mathbb{C}_\Omega : \mathcal{A}_\Omega) : \bar{\epsilon}_M, \text{ and}$$

$$\bar{\sigma} = \bar{\mathbb{C}} : ((1 - f)\mathbb{I}^{(4s)} + f\mathcal{A}_\Omega) : \bar{\epsilon}_M.$$
(9)

Mori–Tanaka's approximation of homogenized stiffness involves using these two expressions to derive

$$\bar{\mathbb{C}} = \left((1 - f) \mathbb{C}_M + f \mathbb{C}_\Omega : \mathcal{A}_\Omega \right) : \left((1 - f) \mathbb{I}^{(4s)} + f \mathcal{A}_\Omega \right)^{-1}. \tag{10}$$

For n distinct phases Ω , this expression becomes

$$\bar{\mathbb{C}} = \left(\sum_{\Omega=0}^{n} f_{\Omega} \mathbb{C}_{\Omega} : \mathcal{A}_{\Omega}\right) : \left(\sum_{\Omega}^{n} f_{\Omega} \mathcal{A}_{\Omega}\right)^{-1}.$$
(11)

In the following subsections in which the Mori–Tanaka approximation is used, the phases which we will homogenize will include the matrix, which includes the cement paste and voids, and the entire composite, which includes the matrix and quartz aggregates.

We note that the Mori–Tanaka approximation is self-consistent: $\bar{\mathbb{C}}^{-1} = \bar{\mathbb{D}}$, where $\bar{\mathbb{D}}$ is the homogenized compliance tensor of the composite. Therefore, while we will take care in evaluating aggregate stresses using Eq. (5) and the knowledge that mixed boundary conditions are applied in our experiments, we may use Eq. (11) to evaluate homogenized sample stiffness, rather than an equivalent expression for $\bar{\mathbb{D}}$, because the two should provide self-consistent results.

3.2. Description of Herve-Zaoui's approximation for homogenized properties

A rigorous method for homogenizing the properties of composites containing layered inclusions (i.e., inclusions composed of more than one concentric phase) was proposed by Herve and Zaoui (1993). The Herve-Zaoui homogenization approach is derived by calculating the average stress and strain in individual phases of a layered-inclusion composite as a function of far-field stresses or strains. The effective bulk and shear moduli of a composite in which an (n-1)-layer inclusion is embedded in a matrix with bulk and shear moduli k_n and μ_n , respectively, can then be calculated and written k^{eff} and μ^{eff} . The effective bulk modulus is given by

$$k^{eff} = k_n^{eff} = k_n + \frac{R_{n-1}^3 / R_n^3}{\frac{1}{k_n^{eff} - k_n} + \frac{3(R_n^3 - R_{n-1}^3)}{R_n^3} \frac{1}{3k_n + 4\mu_n}},$$
(12)

where k_n^{eff} is computed recursively beginning with n=2. The phase fraction of each layer, i, of the inclusion is given by R_i^3/R_n^3 , where n is the number of layers of the inclusions. For a two-phase model (n=2), the effective bulk modulus is equal to the lower (upper) Hashin–Shtrikman bound if the bulk modulus of the matrix is less than (greater than) that of the inclusion (Torquato and Haslach, 2002).

Christensen and Lo have also proposed the three-phase version of Eq. (12), equivalent to the result of Eq. (12) when k_n^{eff} is computed recursively until n=3, to predict the properties of inclusions with one layered embedded within a matrix (Christensen and Lo, 1979). The effective shear modulus in the Herve-Zaoui approach is given by

$$A\left(\frac{\mu^{eff}}{\mu_n}\right)^2 + B\left(\frac{\mu^{eff}}{\mu_n}\right) + C = 0,\tag{13}$$

where A, B, and C are constants described in Appendix.

3.3. Other aspects of the inclusion problem

Another aspect of the inclusion problem not needed in deriving homogenized properties but often used in predicting micro-crack initiation (Mihai and Jefferson, 2011) is the matrix strain field. The matrix strain surrounding an inclusion can be calculated using the exterior point Eshelby tensor, $\mathbb{S}_{Q,F}$, by (Mihai and Jefferson, 2011)

$$\epsilon_{m\Omega}(\mathbf{x}) = \left[\mathbb{I}^{(4s)} + \mathbb{S}_{\Omega,E}(\mathbf{x}) : \mathbb{L}_{\Omega} \right]^{-1} : \epsilon^{\infty}, \tag{14}$$

where $\mathbb{L}_{\Omega}=-[\mathbb{S}_{\Omega}+(\mathbb{D}_{\Omega}-\mathbb{D}_{M})^{-1}:\mathbb{D}_{M}]^{-1}.$ The matrix strain field around inclusions is expected to play an important role in the onset of inelasticity because the stress concentrations generated by the elastic mismatch of inclusions and cement paste or hydrates and cement paste are thought to drive macroscopic fracture nucleation (Königsberger et al., 2014b, 2018). We found the evaluation of these strain fields challenging due to the moderately high density of inclusions and their non-spherical shape. Fig. 9 shows theoretical calculations of matrix strain in a composite subjected to a vertical strain ($\bar{\epsilon}_{zz} = -0.001, \bar{\epsilon}_{xx} =$ $\bar{\epsilon}_{vv} = 0.001v$, with v = 0.23 and other strain tensor values equal to zero) using Eq. (14), matrix properties equal to the properties of cement paste (see Table 3), and a 100 µm radius spherical quartz inclusion. Strains are shown as a function of vertical, d_z , (Fig. 9(a)) and horizontal, d_h , (Fig. 9(b)) distance away from the inclusion center. In future work, we plan to employ spherical inclusions with varying packing fractions and the same DVC procedure employed in this paper to evaluate how closely these theoretical curves match measurements from experiments. This analysis will elucidate the accuracy of theories predicting matrix failure based on exterior Eshelby tensor calculations (Mihai and Jefferson, 2011), will shed light on the role of the elastic mismatch of hydrates and other high-density phases in making strain fields deviate from theoretical values shown in Fig. 9, and may be used to examine inclusion-matrix interfacial properties by comparison to Eshelby theories with interphase effects (e.g., Duan et al. (2007)).

3.4. Experimental comparisons

In this subsection, we compare experimental measurements with predictions of homogenized properties and phase stresses by Mori–Tanaka's and Herve-Zaoui's approximations. Table 2 lists the quantities we compare, their theoretical values, and some details of their experimental computation. We generally assume that far-field tractions were applied to each sample, and employ expressions using $\bar{\sigma}_M$ or $\bar{\sigma}^\infty$ in our micromechanical calculations, where values for $\bar{\sigma}_M$ or $\bar{\sigma}^\infty$ are those shown in Fig. 2. Further details are described in the subsequent subsections.

3.4.1. Mori-Tanaka's and Herve-Zaoui's prediction of homogenized stiffness

This subsection compares Mori–Tanaka's and Herve-Zaoui's approximation of homogenized sample stiffness using with experimental measurements of sample stiffness calculated from the stress–strain curves in Fig. 2(a) (before sample relaxation) (see Table 2, row 1). Both approximations employ phase moduli and phase fractions. Phase fractions are available for each sample from XRCT images and are listed in Table 1. Phase moduli are taken from their values used in prior studies and are shown in Table 3 (Königsberger et al., 2014b; Hurley

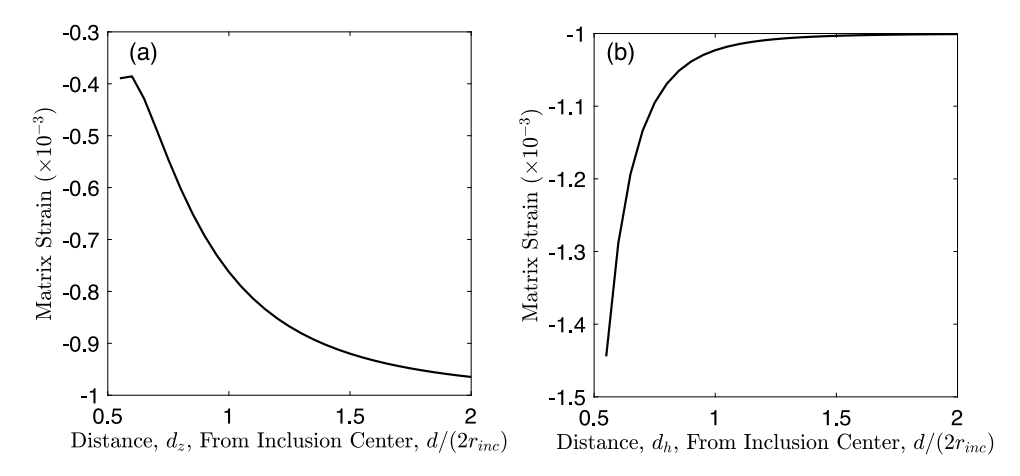


Fig. 9. Matrix strain calculation using Eq. (14) with far-field strains and inclusion sizes described in the text.

Table 2
List of quantities whose theoretical values will be compared with experimental computations.

Quantity	Theory	Input for Theory & Experimental Data to Compare
Mori–Tanaka homogenized stiffness	Eq. (11)	Theory: phase fractions from Table 1 and phase moduli from Table 3 (Königsberger et al., 2014b; Hurley and Pagan, 2019). Data: stiffness from Fig. 2(a), ("Pre") relaxation load cell measurements.
Herve-Zaoui homogenized stiffness	Eqs. (12) and (13)	Theory: phase fractions from Table 1 and phase moduli from Table 3 (Königsberger et al., 2014b; Hurley and Pagan, 2019). Data: stiffness from Fig. 2(a), ("Pre") relaxation load cell measurements.
Mori–Tanaka average aggregate stress	Eq. (5)	Theory: $\bar{\sigma}_M = \sigma^\infty$ from post-relaxation load cell reading. Data: stresses from 3DXRD.
Mori–Tanaka average matrix strain	Eq. (7)	Theory: $\bar{\sigma}_M = \sigma^{\infty}$ from post-relaxation load cell reading or ϵ^{∞} from full-sample DVC registration. Data: average or point-wise DVC in matrix.

Table 3Moduli of each phase fraction from Königsberger et al. (2014b, 2018). The high density phases are assumed to be part of cement paste and are already reflected in the corresponding elastic properties.

Quantity	Bulk modulus, k (GPa)	Shear modulus, g (GPa)
Quartz inclusions	$k_{agg} = 38.1$	$\mu_{agg} = 44.4$
Cement paste	$k_{cem} = 9.88$	$\mu_{cem} = 6.5$
ITZ	$k_{itz} = 8.4$	$\mu_{itz} = 5.53$
Void	$k_v = 0$	$\mu_v = 0$

and Pagan, 2019). A more accurate approach would be to use the phase moduli obtained from nano-indentation experiments performed on each specimen at approximately the same time as the experiments described in Section 2.2. However, such nano-indentation measurements were not performed and experiments on the two samples were performed at times separated by 12 months. We therefore use the phase moduli from prior studies, acknowledging that homogenization results may be only approximate due to drying-induced micro-cracking that may occur over time. In later subsections, we employ the differences between calculated and measured stiffness to infer the amount of damage induced by dry-induced micro-cracking and the effects of other dissipative phenomena. Isotropic linear elastic behavior was assumed for all phases in Table 3, even though minor anisotropy may be present, as is the case for the quartz aggregates (see Section 2.5). The high density phases observed in XRCT images were assumed to be part of the cement paste. The homogenized properties for cement paste in Table 2 are assumed to account for the presence of high-density phases and nano-scale porosity (Königsberger et al., 2014b).

Mori-Tanaka's calculation of homogenized stiffness (called MT) for each of the two samples proceeded as follows. First, we assumed that each sample was composed of two dominant phases, a matrix and quartz inclusions. The matrix was assumed to be composed of cement paste – inclusive of any nano-scale porosity and high-density phases – and large voids. We ignored the presence of ITZ because Mori-Tanaka's theory does not rigorously account for coated inclusions. We therefore added the ITZ volume in Table 1 to that of the cement paste, bringing the total cement paste volume fraction to 0.81 for Sample 1 and 0.82 for Sample 2. The homogenized matrix properties were calculated using Eq. (11) assuming two phases: cement paste and voids. The cement paste volume fraction of the matrix was taken as $f_{cp}^{(MT)} = f_{cp}/(f_{cp} + f_v)$ and the large void volume fraction was taken as $f_v^{(MT)} = f_v/(f_{cp} + f_v)$. Following homogenization for matrix stiffness, homogenized sample properties were calculated using Eq. (11) assuming two phases, matrix and quartz inclusions. The matrix volume fraction was assumed to be the sum of the cement paste, ITZ, and large voids in Table 1: 0.82 for Sample 1 and 0.85 for Sample 2. The inclusion volume fraction was 0.18 for Sample 1 and 0.15 for Sample 2. The procedure for calculating the MT approximation is summarized in Table 4.

Herve-Zaoui's calculation of homogenized stiffness (called HZ) for each of the two samples proceeded as follows. First, we assume that each sample is a four-phase composite: a two-layer inclusion, composed of a quartz aggregate surrounded by a layer of ITZ, embedded in a matrix that is itself embedded in a mean field. The radii, R_1 , R_2 , and R_3 of the inclusion, ITZ, and matrix, respectively, are taken such that $(R_1/R_n)^3$ represents the inclusion volume fraction of each sample in Table 1 and $(R_2/R_3)^3$ represents the ITZ volume fraction of each sample

Table 4 Mori–Tanaka and Herve-Zaoui approximations for Young's modulus, E, for Samples 1 and 2. f_p is the phase fraction of phase p, where p=0 is for cement paste, p=1 is for void, p=2 is for quartz inclusions, and p=3 is for the homogenized matrix. \mathbb{C}_p is the stiffness tensor of phase p. \mathcal{A}_p is the concentration tensor for phase p.

Approx.	Description
MT	Matrix: cement paste and void $\mathbb{C}_m = \left(\sum_{p=0}^1 f_p \mathbb{C}_p : A_p\right) : \left(\sum_{p=0}^1 f_p A_p\right)^{-1};$
	Inclusion: aggregate and ITZ, $\mathbb{C}_{inc} = \left(\sum_{p=2}^{3} f_p \mathbb{C}_p : A_p\right) : \left(\sum_{p=2}^{3} f_p A_p\right)^{-1}$.
	Each homogenized using phase fractions from Table 1. Final homogenization with
	Eq. (11),
	$\bar{\mathbb{C}} = \left(f_m \mathbb{C}_m : \mathcal{A}_m + f_{inc} \mathbb{C}_{inc} : \mathcal{A}_{inc} \right) : \left(f_m \mathcal{A}_m + f_{inc} \mathcal{A}_{inc} \right)^{-1}.$
HZ	Matrix: cement paste and void $\mathbb{C}_m = \left(\sum_{p=0}^1 f_p \mathbb{C}_p : A_p\right) : \left(\sum_{p=0}^1 f_p A_p\right)^{-1}$,
	homogenized as described in the text.
	Inclusion: quartz inclusion with layer of ITZ.
	Final homogenization with Eqs. (12) and (13).

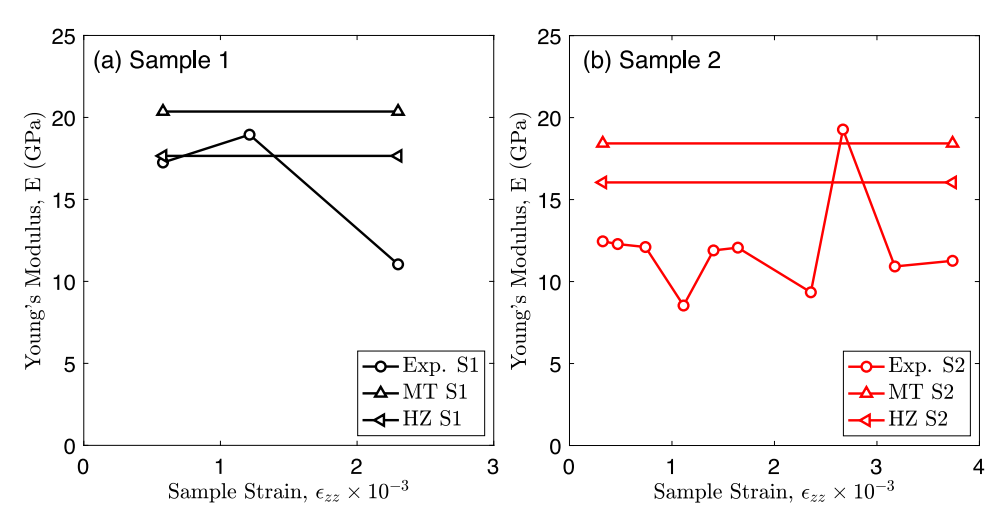


Fig. 10. A comparison of the Mori-Tanaka and Herve-Zaoui approximations for sample stiffness, described in the text, and the experimental results for Samples 1 (a) and 2 (b). The Exp. S1 and Exp. S2 labels refer to experimental results for Samples 1 (S1) and 2 (S2).

Table 5 Mori–Tanaka and Herve-Zaoui approximations for Young's modulus, $\it E$, for Samples 1 and 2.

Sample	Exp. Mean \pm Std. (GPa)	MT (GPa)	HZ (GPa)
1	15.75 ± 4.16	21.86	17.84
2	12.02 ± 2.87	20.95	17.12

in Table 1. The quartz inclusion and ITZ properties used in the Herve-Zaoui calculation are taken from Table 3. The matrix properties are assumed to be those homogenized by a Mori–Tanaka calculation similar to the one described in the previous paragraph, taking into account the presence of cement paste (now without ITZ added to its volume fraction) and large voids. Eqs. (12) and (13) are then employed to render the HZ approximation, as summarized in Table 4.

Results of the MT and HZ calculations are shown in Table 5 and Fig. 10. Experimental Young's moduli are calculated by dividing the change in stress before relaxation (see Fig. 2) by the strain between those load steps. The resulting moduli are plotted at the second of the sequential strains across which they are calculated in Fig. 10.

For Sample 1, the MT and HZ approximations provide stiffness predictions that agree reasonably-well with experimental measurements during the first two load steps of the experiment, as shown in Fig. 10(a). The HZ approximation agrees with experimental measurements more closely. Neither the MT nor the HZ approximations match experimental measurements well for the third load step of the experiment on Sample 1. Fracture nucleation is visible in this third load step upon careful inspection of XRCT images, as discussed in Hurley and Pagan (2019).

This fracturing explains the significant reduction in sample stiffness and over-prediction of MT and HZ calculations.

For Sample 2, the MT and HZ approximations over-predict sample stiffness for all load steps except for load step 8. We believe this discrepancy may arise from several factors: (1) inaccurate matrix properties due to drying-induced micro-cracking in the cement paste; (2) the use of elastic moduli rather than more complex and possibly more accurate visco-elasto-viscoplastic loading moduli (Irfan-ul Hassan et al., 2016); (3) a change in representative length scale because Sample 2 contains fewer and larger inclusions. We rule out the third of these factors because, although there are fewer and larger inclusions in Sample 2, the 1 mm side-length of the sample remains greater than twice the largest inclusion dimension, which is the minimum size determined by prior studies to constitute an RVE exhibiting 5% error in modulus (Drugan and Willis, 1996). We therefore conclude that the discrepancy is due to either drying-induced micro-cracking or the use of elastic moduli rather than visco-elasto-viscoplastic loading moduli. As noted by other authors, such visco-elasto-viscoplastic loading moduli are relevant whenever moduli are derived from stress-strain protocols (Irfan-ul Hassan et al., 2016). These visco-elasto-viscoplastic moduli are associated with dissipative phenomena, potentially including sliding on micro-cracks. The distinction between the effects of micro-cracks and the use of elastic rather than visc-elasto-viscoplastic moduli is therefore not particularly meaningful in the absence of additional information because they are related. Nevertheless, we exploit the discrepancy between theory and measurements in Section 3.4.4 to derive an effective empirical damage constant.

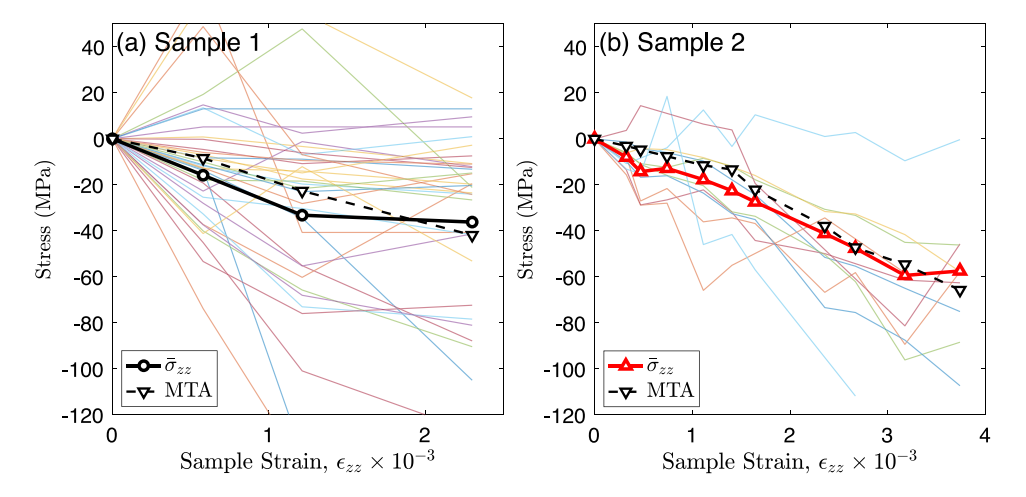


Fig. 11. A comparison of individual quartz inclusion stresses (thin curves) and average inclusion stresses (thick solid lines) with Mori-Tanaka predictions (thick dashed lines, labeled MTA) using Eq. (3) for Sample 1 (a) and Sample 2 (b), as described in the text.

3.4.2. Mori-Tanaka prediction of average inclusion stress

This subsection compares Mori–Tanaka's prediction of average inclusion stresses using Eq. (5) with experimental measurements of quartz inclusion stresses made using 3DXRD and shown in Figs. 7 and 8. Far-field traction boundary conditions were assumed, with the σ_{zz}^∞ component of far-field stress being the macroscopic stress measured during 3DXRD scans ("Post" symbols in Fig. 2(b)). This is the natural stress to use in theoretical calculations as this is the far-field stress on the sample when the 3DXRD measurements are made. All other far-field stress tensor components were taken to be zero, consistent with the lateral surfaces of samples being unconfined.

Average inclusion stresses, shown in Fig. 7, are reproduced in Fig. 11. The thin curves in Fig. 11 convey the stresses in each aggregate as a function of macroscopic strain while thick solid curves convey the averages to be compared with the calculations using Eq. (5). The Mori-Tanaka prediction, labeled MTA, is shown in dashed lines. For both Samples 1 and 2, the individual aggregate stresses vary significantly through the elastic stage of the experiments, as also discussed in our prior work (Hurley and Pagan, 2019). The volume-average stresses, on the other hand, increase smoothly and are closely predicted the Mori-Tanaka approximation. For both samples, the Mori-Tanaka predictions match the average aggregate stresses very closely. The close agreement between theory and experiments in Fig. 11 leads us to conclude with direct measurements that the average aggregate stresses underlying the Mori-Tanaka homogenization process are very accurate for cementitious composites. Further discussion of this finding is provided in Section 3.4.4, when we recalculate these average aggregate stresses under the assumption of a damaged matrix.

3.4.3. Mori-Tanaka prediction of average matrix strain

We next compare Mori–Tanaka predictions of average cement paste strain using Eq. (7) with DVC calculations made on XRCT images. To make this comparison, we first calculate the average strain throughout the matrix of each sample using DVC measurements made at each load step. We do not consider strains for which any portion of a DVC correlation window overlaps an aggregate particle, large voids, the top or bottom piston contacting the sample, or the void space outside of the sample. In practice, this is accomplished by ignoring DVC results centered on points within about 31 μm of quartz inclusions, or about $18\sqrt{3}~\mu m$, where 18 is the DVC half-window size and $\sqrt{3}$ accounts for the cubic shape of correlation windows. The average matrix strain calculated from DVC is compared to theoretical predictions of \bar{e}_M . Because we assumed far-field stress boundary conditions in prior subsections, we first calculate the Mori–Tanaka approximation for \bar{e}_M by $\bar{e}_M = \mathbb{C}_M^{-1}$: $\bar{\sigma}^\infty$, where $\bar{\sigma}^\infty$ is the sample stress after sample strain

("Pre" in Fig. 2) and \mathbb{C}_M is the homogenized matrix stiffness calculated using Eq. (11) and described in Section 3.4.1. We call the result MTM1. Using $\bar{\sigma}^{\infty}$ as the sample stress during 3DXRD measurements yielded similar results. Because we could also have assumed far-field displacement boundary conditions, we can also calculate the Mori–Tanaka approximation for $\bar{\epsilon}_M$ by $\bar{\epsilon}_M = \bar{\epsilon}^{\infty}$, where $\bar{\epsilon}^{\infty}$ is the value of strain calculated from full-image XRCT registration, the zz component of which is shown in Fig. 2. We call this result MTM2.

A comparison of average matrix strains calculated through Mori–Tanaka's approximation and from experimental data is shown in Fig. 12. The MTM2 calculation provides a closer match to the experimental data than the MTM1 calculation for both Samples 1 and 2 for all load steps. It is noteworthy that MTM1 provides a particularly poor prediction for matrix strains in Sample 2, suggesting that the assumption of a mean field with stiffness \mathbb{C}_M is particularly poor for this sample. This motivates our attempt to degrade the stiffness of the matrix using a scalar damage value in the next subsection.

3.4.4. Estimation of damage from drying-induced micro-cracking

In this subsection, we use the discrepancy between MT and HZ approximations and experimental stiffness measurements from Section 3.4.1 to estimate the damage in Samples 1 and 2 from drying-induced micro-cracking. In particular, after calculating the homogenized matrix stiffness \mathbb{C}_M using the nominal properties of the cement paste provided in Table 2, as described in Section 3.4.1, we use a simple scalar damage variable D, ranging from 0 to 1, and adjust \mathbb{C}_M according to

$$\tilde{\mathbb{C}}_{M} = (1 - D)\mathbb{C}_{M}.\tag{15}$$

D is found by simple trial and error by adjusting D until the MT and HZ approximations visually match the majority of the experimental stiffness measurements. A value of D = 0.05 was found to be appropriate for Sample 1 and a value of D = 0.35 was found to be appropriate for Sample 2. The resulting MT and HZ macroscopic stiffness predictions, calculated as described in Section 3.4.1 using $\tilde{\mathbb{C}}_M$ rather than \mathbb{C}_M , are shown in Fig. 13. The relative values of D in Samples 1 and 2 is consistent with increasing apparent matrix damage due to dryinginduced micro-cracking. We note that more complex procedures may be employed, which make use of crack density parameters within homogenization procedures to capture stiffness degradation due to damage (e.g., Pensée et al., 2002; Deude et al., 2002; Jagsch et al., 2020; Scheiner et al., 2016). We choose not to pursue these approaches here because, as noted at the end of Section 3.4.1, it is likely not possible to distinguish between the presence of micro-cracks and other effects that give rise to visco-elasto-viscoplastic moduli that emerge

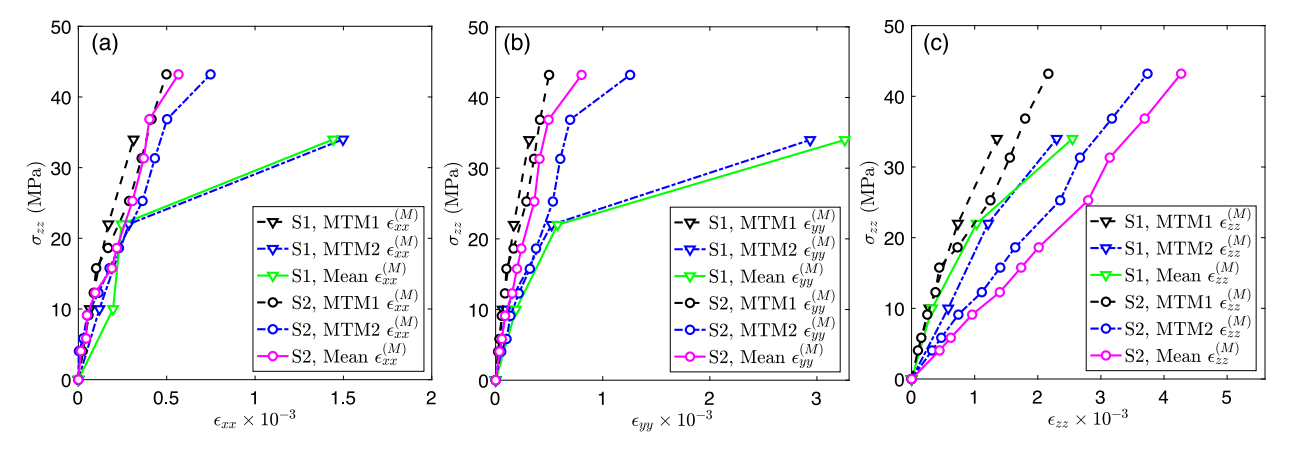


Fig. 12. A comparison of (a) $\bar{\epsilon}_{xx}$, (b) $\bar{\epsilon}_{yy}$, and (c) $\bar{\epsilon}_{zz}$ predicted by Mori–Tanaka assumptions MTM1 and MTM2 (described in the main text) and DVC results (called "Mean" in the legend) for Sample 1 (S1) and Sample 2 (S2) as a function of macroscopic far-field sample stress, σ_{zz} . Note: strain is plotted on the *x*-axis for consistency with Fig. 2 and typical stress–strain curves, even though σ_{zz} is not the dependent variable of interest in the plot.

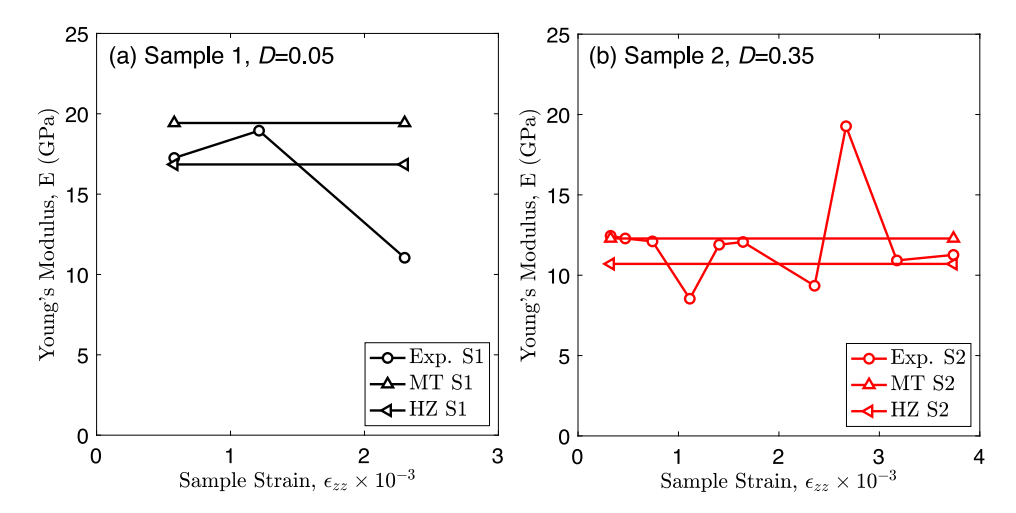


Fig. 13. MT and HZ approximations for sample stiffness using a reduced matrix stiffness to reflect the effects of drying-induced micro-cracking.

from analysis of stress–strain curves. We therefore associate damage and ${\it D}$ with a combination of micro-cracking and any other dissipative phenomena.

It is interesting to note that damage effects do not noticeably influence the MTA prediction of average inclusion stress. In Fig. 14 we reproduce the comparison of individual average inclusion stresses with Mori–Tanaka predictions, with the latter computed using $\tilde{\mathbb{C}}_M$ rather than \mathbb{C}_M . The significant stiffness mismatch between the matrix and inclusions, present in both the damaged and undamaged cases, likely accounts for the almost indiscernible change in the MTA prediction between Figs. 14 versus 11.

Damage effects do have a noticeable influence on the MTM1 predictions of average matrix strain shown in Fig. 9. We reproduce these results in Fig. 15, which conveys that MTM1 approaches MTM2 predictions for most load steps for both samples, except the third load step for Sample 1. This implies that the matrix properties captured in $\tilde{\mathbb{C}}_M$ are now more representative of the mean field in both samples.

4. Discussion

We quantitatively examined three aspects of Mori–Tanaka's and Herve-Zaoui's approximation using experimental data from two samples of cementitious composites made with Portland cement and quartz inclusions. The first aspect of the approximations we examined, the homogenized stiffness itself, was accurate for one sample and inaccurate for another (Fig. 10), despite using nearly identical methods for

experimental data analysis and the same phase moduli Mori–Tanaka calculations. Ruling out a change in representative length scale for Sample 2, we concluded that the likely cause of the inaccuracy was drying-induced micro-cracking or other dissipative processes which tend to cause discrepancies between predictions made with elastic moduli and stiffness derived from stress–strain curves (the latter relates more to visco-elasto-viscoplastic moduli (Irfan-ul Hassan et al., 2016)).

Inclusion stresses were the second aspect of Mori–Tanaka's approximation that we examined with our experimental data (Fig. 11). It was remarkable that predictions of inclusion stresses for the both samples were accurate despite the inaccuracy of the stiffness prediction for the second sample. This likely arises because predictions of inclusion stresses are insensitive to changes in matrix stiffness when the contrast between matrix and inclusion stiffness is large, as in our samples. This claim was supported by the observation in Section 3.4.4 that reducing the matrix stiffness by 35% to capture the effect of drying-induced micro-cracking and other dissipative effects did not significantly influence average inclusion stress predictions.

The third aspect of Mori–Tanaka's approximation that we examined was the average matrix strain. The average matrix strain in the first sample we examined was predicted well with Mori–Tanaka's assumption that $\bar{\epsilon}_M = \epsilon^\infty$, i.e., that the mean-field surrounding inclusions has the properties of the matrix, at least in the first two load steps in which the sample remained largely free of fractures. However, the average matrix strain in the second sample was not predicted well with Mori–Tanaka's assumption. Widespread drying-induced micro-cracking

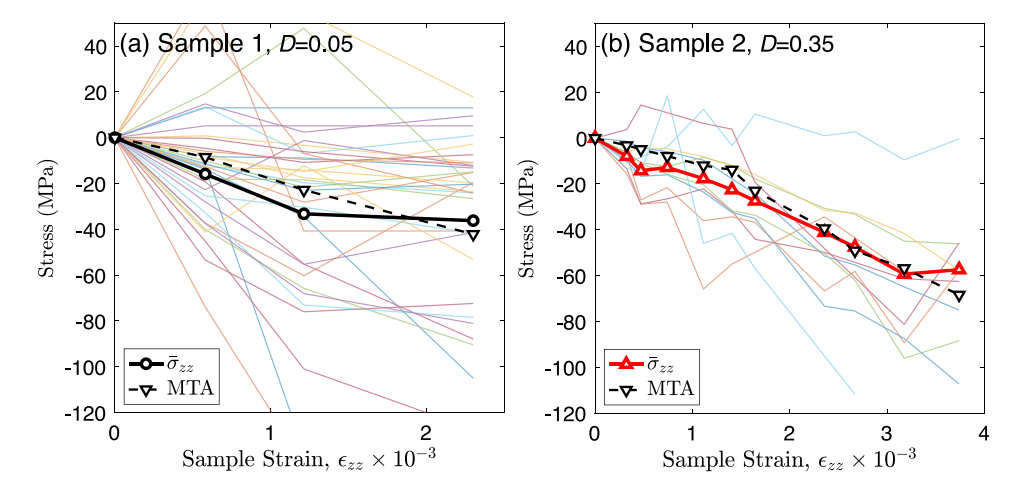


Fig. 14. A comparison of individual quartz inclusion stresses (thin curves) and average inclusion stresses (thick solid lines) with Mori-Tanaka predictions (thick dashed lines, labeled MTA) using Eq. (3) for Sample 1 (a) and Sample 2 (b), as described in the text. A damaged matrix was assumed, with damage values provided in the plots and described in the text.

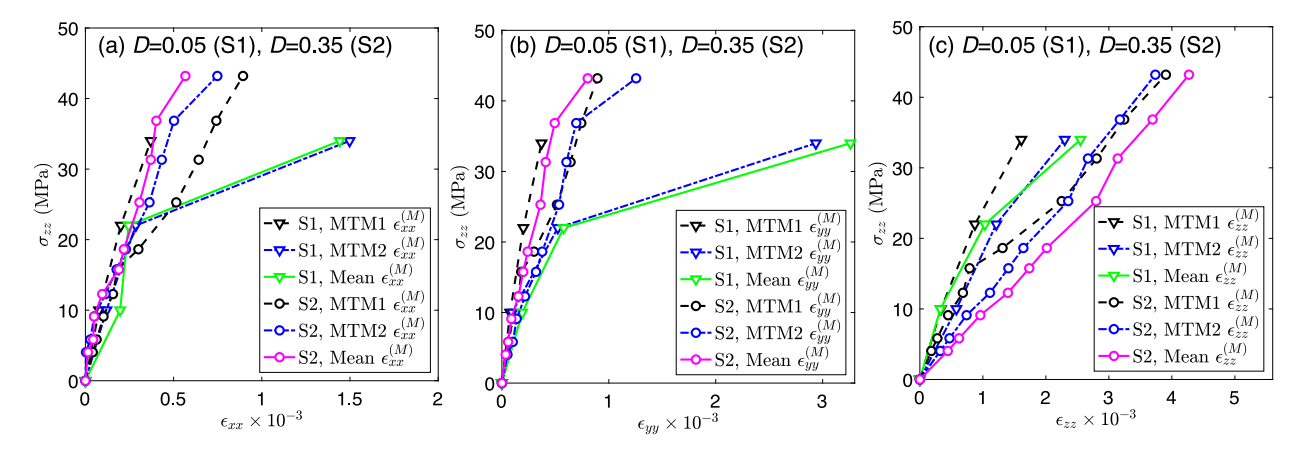


Fig. 15. A comparison of (a) $\bar{\epsilon}_{xx}$, (b) $\bar{\epsilon}_{yy}$, and (c) $\bar{\epsilon}_{zz}$ predicted by Mori–Tanaka assumptions MTM1 and MTM2 (described in the main text) and DVC results (called "Mean" in the legend) for Sample 1 (S1) and Sample 2 (S2) as a function of macroscopic far-field sample stress, σ_{zz} . Note: strain is plotted on the *x*-axis for consistency with Fig. 2 and typical stress–strain curves, even though σ_{zz} is not the dependent variable of interest in the plot. A damaged matrix is assumed for both samples, with D=0.05 for Sample 1 and D=0.35 for Sample 2. The damaged matrix properties are computed using Eq. (15).

for this sample, which aged at room temperature 12 months longer than the first sample, as well as other dissipative phenomena upon loading was assumed to be the cause for this discrepancy.

A simple calculation revealed that a scalar damage variable could be used to capture the drying-induced micro-cracking and other dissipative effects in both samples studied in this paper. The increase in damage from the first to second sample is consistent with a longer aging time at room temperature. To more definitively validate our conclusion that micro-cracking is the cause of reduced stiffness for the second sample we studied, we propose future experiments that incorporate nano-indentation immediately prior to mechanical testing (Ulm et al., 2004). We further propose for future work the investigation of whether an analytical or numerical model of drying-induced micro-cracking may quantitatively explain the observed reduction in sample stiffness and changes in average matrix strains.

5. Conclusion

We used theoretical calculations and *in-situ* X-ray measurements made on two cementitious composite samples to examine continuum micromechanics theories for these materials. By combining XRCT, 3DXRD, and DVC, we were able to quantitatively examine sample stiffness, inclusion stresses, and matrix strain. Sample stiffness predicted by Mori–Tanaka's approximation matched experimental measurements

for one of the two samples. For the sample that did not match, further analysis of 3DXRD and DVC data revealed that the linear-elastic micromechanics models are not elaborate enough to reproduce results from a test in which time-dependent and inelastic deformation took place. Interestingly, inclusion stresses in both samples were predicted accurately, as long as uniform stress boundary conditions were used and the associated stress was assumed to be the macroscopic sample stress measured during 3DXRD scans.

Our analysis and discussion lead to several conclusions:

- Continuum micromechanics theories like Mori–Tanaka's approximation can accurately predict the homogenized stiffness of cementitious composites with millimeter length scales and inclusions measuring several hundred microns in dimension.
- The inclusion stresses predicted by Mori–Tanaka's approximation can be accurate for cementitious composites even when homogenized stiffness predictions are inaccurate because of a damaged matrix phase or inaccurate matrix moduli.
- The assumption of a mean-field surrounding inclusions with properties furnished by the matrix may be inaccurate for some cementitious composites featuring drying-induced micro-cracking or other dissipative phenomena. A mean-field with more accurate properties can be obtained with a simple scalar damage variable accounting for micro-cracking and dissipative phenomena in some cases.

$$\boldsymbol{M}^{(k)} = \frac{1}{5(1-v_{k+1})} \begin{bmatrix} \frac{c_k}{3} & \frac{R_k^2(3b_k-7c_k)}{5(1-2v_k)} & \frac{-12\alpha_k}{R_k^5} & \frac{4(f_k-27\alpha_k)}{15(1-2v_k)R_k^3} \\ 0 & \frac{(1-2v_{k+1})b_k}{7(1-2v_k)} & \frac{-20(1-2v_{k+1})\alpha_k}{7R_k^7} & \frac{-12\alpha_k(1-2v_{k+1})}{7(1-2v_k)R_k^5} \\ \frac{R_k^5\alpha_k}{2} & \frac{-R_k^7(2a_k+147\alpha_k)}{70(1-2v_k)} & \frac{d_k}{7} & \frac{R_k^2(105(1-v_{k+1})+12\alpha_k(7-10v_{k+1})-7e_k)}{35(1-2v_k)} \\ -\frac{5}{6}(1-2v_{k+1})\alpha_k R_k^3 & \frac{7(1-2v_{k+1})\alpha_k R_k^5}{2(1-2v_k)} & 0 & \frac{e_k(1-2v_{k+1})}{3(1-2v_k)} \end{bmatrix}$$

Box I.

 The measurements and analysis presented here provide future opportunities for studying the micromechanics of cementitious composites and assessing the microscale causes for their deviations from experimental measurements. This information can be used to provide insight into predictions of elasticity and inelasticity.

Declaration of competing interest

The authors declare that they have no known competing financial interests or personal relationships that could have appeared to influence the work reported in this paper.

Data availability

Data will be made available on request.

Acknowledgments

RCH and CZ acknowledge support from the Johns Hopkins University's Whiting School of Engineering, USA. RCH acknowledges support from the U.S. National Science Foundation Award No. CMMI-2125023. RCH, EBH, and CZ acknowledge support for the load frame construction from Lawrence Livermore National Laboratory's Laboratory Directed Research and Development (LDRD), USA program under grant 17-LW-009. Part of this work is based upon research conducted at the Cornell High Energy Synchrotron Source (CHESS) which is supported by the National Science Foundation (NSF), USA and the National Institutes of Health/National Institute of General Medical Sciences, USA under NSF award DMR-133208. We also acknowledge the APS for synchrotron beamtime under proposal GUP-59127. Use of the APS, an Office of Science User Facility operated for the US Department of Energy (DOE) Office of Science by Argonne National Laboratory, was supported by US DOE Contract DE-AC02-06CH11357. We thank Dr. J. Almer, Dr. P. Kenesei, and Dr. J.S. Park for help in executing one of the experiments in this paper. We thank Dr. Ghassan Shahin, Dr. Mohmad Mohsin Thakur, Arthur Ding, and Ziheng Wang for useful discussions.

Appendix. Herve-zaoui's approximation for shear modulus

In the main text, the effective shear modulus in the Herve-Zaoui approach is given by

$$A\left(\frac{\mu^{eff}}{\mu_n}\right)^2 + B\left(\frac{\mu^{eff}}{\mu_n}\right) + C = 0, \tag{A.1}$$

where A, B, and C are constants. We direct the reader to Herve and Zaoui (1993) for a full derivation and explanation of the constants.

Here, we simply show them for the n = 3 model described in the main text for completeness. The constants A, B, and C are given by

$$\begin{split} A = &4R_3^{10}(1-2v_3)(7-10v_3)Z_{12} + 20R_3^7(7-12v_3+8v_3^2)Z_{42} \\ &+12R_3^5(1-2v_3)... \\ &\times (Z_{14}-7Z_{23}) + 20R_3^3(1-2v_3)^2Z_{13} + 16(4-5v_3)(1-2v_3)Z_{43}, \\ B = &3R_3^{10}(1-2v_3)(15v_3-7)Z_{12} + 60R_3^7(v_3-3)v_3Z_{42} - 24R_3^5(1-2v_3)... \\ &\times (Z_{14}-7Z_{23}) - 40R_3^3(1-2v_3)^2Z_{13} - 8(1-5v_3)(1-2v_3)Z_{43}, \\ C = &-R_3^{10}(1-2v_3)(7+5v_3)Z_{12} + 10R_3^7(7-v_3^2)Z_{43} + 12R_3^5(1-2v_3)... \\ &\times (Z_{14}-7Z_{23}) + 20R_3^3(1-2v_3)^2Z_{13} - 8(7-5v_3)(1-2v_3)Z_{43}, \end{split}$$

with R_3 described in the main text, v_3 the Poisson's ratio of the matrix, Z_{ii} given by

$$Z_{ij} = P_{i1}^{(3)} P_{i2}^{(3)} - P_{i1}^{(3)} P_{i2}^{(3)}, \tag{A.3}$$

and $P^{(3)} = M^{(1)}M^{(2)}$, where M^1 and M^2 are defined in Eq. (A.4) given in Box I. The constants in Eq. (A.4) are given by

$$a_{k} = \frac{\mu_{k}}{\mu_{k+1}} (7 + 5\nu_{k})(7 - 10\nu_{k+1}) - (7 - 10\nu_{k})(7 + 5\nu_{k+1}),$$

$$b_{k} = 4(7 - 10\nu_{k}) + \frac{\mu_{k}}{\mu_{k+1}} (7 + 5\nu_{k}),$$

$$c_{k} = (7 - 5\nu_{k+1}) + 2\frac{\mu_{k}}{\mu_{k+1}} (4 - 5\nu_{k+1}),$$

$$d_{k} = (7 + 5\nu_{k+1}) + 4\frac{\mu_{k}}{\mu_{k+1}} (7 - 10\nu_{k+1}),$$

$$e_{k} = 2(4 - 5\nu_{k}) + \frac{\mu_{k}}{\mu_{k+1}} (7 - 5\nu_{k}),$$

$$f_{k} = (4 - 5\nu_{k})(7 - 5\nu_{k+1}) - \frac{\mu_{k}}{\mu_{k+1}} (4 - 5\nu_{k+1})(7 - 5\nu_{k}),$$

$$\alpha_{k} = \frac{\mu_{k}}{\mu_{k+1}} - 1,$$
(A.5)

where μ_k is the shear modulus of phase k.

References

Benveniste, Y., 1987. A new approach to the application of Mori-Tanaka's theory in composite materials. Mech. Mater. 6 (2), 147–157.

Bernier, J., Barton, N., Lienert, U., Miller, M., 2011. Far-field high-energy diffraction microscopy: a tool for intergranular orientation and strain analysis. J. Strain Anal. Eng. Des. 46 (7), 527–547.

Champley, K., 2016. Livermore Tomography Tools (LTT) Technical Manual. Tech. rep., LLNL Technical Report under development, (Dec 11, 2015).

Christensen, R.M., 1990. A critical evaluation for a class of micro-mechanics models. J. Mech. Phys. Solids 38 (3), 379–404.

Christensen, R., Lo, K., 1979. Solutions for effective shear properties in three phase sphere and cylinder models. J. Mech. Phys. Solids 27 (4), 315–330.

Deude, V., Dormieux, L., Kondo, D., Maghous, S., 2002. Micromechanical approach to nonlinear poroelasticity: application to cracked rocks. J. Eng. Mech. 128 (8), 848–855.

Drugan, W.J., Willis, J.R., 1996. A micromechanics-based nonlocal constitutive equation and estimates of representative volume element size for elastic composites. J. Mech. Phys. Solids 44 (4), 497–524.

Duan, H., Yi, X., Huang, Z., Wang, J., 2007. A unified scheme for prediction of effective moduli of multiphase composites with interface effects. Part I: Theoretical framework. Mech. Mater. 39 (1), 81–93.

- Eshelby, J.D., 1957. The determination of the elastic field of an ellipsoidal inclusion, and related problems. Proc. R. Soc. Lond. Ser. A. Math. Phys. Sci. 241 (1226), 376–396.
- Ferrari, M., 1991. Asymmetry and the high concentration limit of the Mori-Tanaka effective medium theory. Mech. Mater. 11 (3), 251–256.
- Fischer, I., Pichler, B., Lach, E., Terner, C., Barraud, E., Britz, F., 2014. Compressive strength of cement paste as a function of loading rate: Experiments and engineering mechanics analysis. Cem. Concr. Res. 58, 186–200.
- Gürsoy, D., De Carlo, F., Xiao, X., Jacobsen, C., 2014. TomoPy: a framework for the analysis of synchrotron tomographic data. J. Synchrotron Radiat. 21 (5), 1188–1193
- Hashin, Z., 1991. The spherical inclusion with imperfect interface. J. Appl. Mech. 2 (58), 444-449.
- Irfan-ul Hassan, M., Pichler, B., Reihsner, R., Hellmich, C., 2016. Elastic and creep properties of young cement paste, as determined from hourly repeated minute-long quasi-static tests. Cem. Concr. Res. 82, 36–49.
- Herve, E., Zaoui, A., 1993. N-layered inclusion-based micromechanical modelling. Internat. J. Engrg. Sci. 31 (1), 1–10.
- Hild, F., Roux, S., Bernard, D., Hauss, G., Rebai, M., 2013. On the use of 3D images and 3D displacement measurements for the analysis of damage mechanisms in concrete-like materials. In: VIII International Conference on Fracture Mechanics of Concrete and Concrete Structures FraMCoS-8. Tolede, Spain, URL https://hal. archives-ouvertes.fr/hal-01385670.
- Hurley, R.C., 2021. Stress and force measurement uncertainties in 3D granular materials. In: EPJ Web of Conferences, Vol. 249. EDP Sciences, p. 02009.
- Hurley, R., Hall, S., Andrade, J., Wright, J., 2016. Quantifying interparticle forces and heterogeneity in 3D granular materials. Phys. Rev. Lett. 117 (9), 098005.
- Hurley, R.C., Herbold, E.B., Pagan, D.C., 2018. Characterization of the crystal structure, kinematics, stresses and rotations in angular granular quartz during compaction. J. Appl. Crystallogr. 51 (4).
- Hurley, R., Pagan, D., 2019. An in-situ study of stress evolution and fracture growth during compression of concrete. Int. J. Solids Struct. 168, 26–40.
- Jagsch, V., Kuttke, P., Lahayne, O., Zelaya-Lainez, L., Scheiner, S., Hellmich, C., 2020. Multiscale and multitechnique investigation of the elasticity of grooved rail steel. Constr. Build. Mater. 238, 117768.
- Klusemann, B., Böhm, H., Svendsen, B., 2012. Homogenization methods for multi-phase elastic composites with non-elliptical reinforcements: Comparisons and benchmarks. Eur. J. Mech. A Solids 34, 21–37.
- Königsberger, M., Hlobil, M., Delsaute, B., Staquet, S., Hellmich, C., Pichler, B., 2018. Hydrate failure in ITZ governs concrete strength: A micro-to-macro validated engineering mechanics model. Cem. Concr. Res. 103, 77–94.
- Königsberger, M., Pichler, B., Hellmich, C., 2014a. Micromechanics of ITZ-aggregate interaction in concrete part I: stress concentration. J. Am. Ceram. Soc. 97 (2), 535–542.
- Königsberger, M., Pichler, B., Hellmich, C., 2014b. Micromechanics of ITZ-aggregate interaction in concrete part II: Strength upscaling. J. Am. Ceram. Soc. 97 (2), 543–551.
- Königsberger, M., Pichler, B., Hellmich, C., 2020. Multiscale poro-elasticity of densifying calcium-silicate hydrates in cement paste: an experimentally validated continuum micromechanics approach. Internat. J. Engrg. Sci. 147, 103196.
- Li, S., Wang, G., 2008. Introduction To Micromechanics and Nanomechanics. World Scientific Publishing Company.
- Loeffler, C.M., Qiu, Y., Martin, B., Heard, W., Williams, B., Nie, X., 2018. Detection and segmentation of mechanical damage in concrete with X-Ray microtomography. Mater. Charact. 142, 515–522.
- Lucas, B.D., Kanade, T., 1981. An iterative image registration technique with an application to stereo vision. In: Proceedings of the International Joint Conference on Artificial Intelligence. Vancouver, British Columbia, pp. 674–679.
- Mao, L., Yuan, Z., Yang, M., Liu, H., Chiang, F.-p., 2019. 3D strain evolution in concrete using in situ X-ray computed tomography testing and digital volumetric speckle photography. Measurement 133, 456–467.
- Mayo, S.C., Davis, T.J., Gureyev, T.E., Miller, P.R., Paganin, D., Pogany, A., Stevenson, A.W., Wilkins, S., 2003. X-ray phase-contrast microscopy and microtomography. Opt. Express 11 (19), 2289–2302.
- Mihai, I.C., Jefferson, A.D., 2011. A material model for cementitious composite materials with an exterior point Eshelby microcrack initiation criterion. Int. J. Solids Struct. 48 (24), 3312–3325.
- Mondal, P., Shah, S., Marks, L., 2009. Nanomechanical properties of interfacial transition zone in concrete. In: Nanotechnology in Construction 3. Springer, pp. 315–320.
- Mori, T., Tanaka, K., 1973. Average stress in matrix and average elastic energy of materials with misfitting inclusions. Acta Metall. 21 (5), 571-574.
- Nair, S.D., Nygren, K.E., Pagan, D.C., 2019. Micromechanical response of crystalline phases in alternate cementitious materials using 3-dimensional X-ray techniques. Sci. Rep. 9 (1), 1–12.

- Nemat-Nasser, S., Hori, M., 2013. Micromechanics: Overall Properties of Heterogeneous Materials. Elsevier.
- Oddershede, J., Schmidt, S., Poulsen, H.F., Sørensen, H.O., Wright, J., Reimers, W., 2010. Determining grain resolved stresses in polycrystalline materials using three-dimensional X-ray diffraction. J. Appl. Crystallogr. 43 (3), 539–549.
- Park, J.-S., Zhang, X., Sharma, H., Kenesei, P., Hoelzer, D., Li, M., Almer, J., 2015. High-energy synchrotron x-ray techniques for studying irradiated materials. J. Mater. Res. 30 (9), 1380–1391.
- Pensée, V., Kondo, D., Dormieux, L., 2002. Micromechanical analysis of anisotropic damage in brittle materials. J. Eng. Mech. 128 (8), 889–897.
- Pichler, B., Dormieux, L., 2008. Consistency of homogenization schemes in linear poroelasticity. Compt. R. Mec. 336 (8), 636–642.
- Pichler, B., Hellmich, C., 2011. Upscaling quasi-brittle strength of cement paste and mortar: A multi-scale engineering mechanics model. Cem. Concr. Res. 41 (5), 467–476.
- Poulsen, H.F., 2004. Three-Dimensional X-Ray Diffraction Microscopy: Mapping Polycrystals and their Dynamics, Vol. 205. Springer Science & Business Media.
- Ramesh, G., Sotelino, E., Chen, W., 1996. Effect of transition zone on elastic moduli of concrete materials. Cem. Concr. Res. 26 (4), 611–622.
- Ramesh, G., Sotelino, E., Chen, W.-F., 1998. Effect of transition zone on elastic stresses in concrete materials. J. Mater. Civ. Eng. 10 (4), 275–282.
- Scheiner, S., Komlev, V.S., Hellmich, C., 2016. Strength increase during ceramic biomaterial-induced bone regeneration: a micromechanical study. Int. J. Fract. 202, 217–235.
- Scrivener, K.L., Crumbie, A.K., Laugesen, P., 2004. The interfacial transition zone (ITZ) between cement paste and aggregate in concrete. Interface Sci. 12 (4), 411–421.
- Sevostianov, I., Kachanov, M., 2014. On some controversial issues in effective field approaches to the problem of the overall elastic properties. Mech. Mater. 69 (1), 93-105.
- Shade, P.A., Blank, B., Schuren, J.C., Turner, T.J., Kenesei, P., Goetze, K., Suter, R.M., Bernier, J.V., Li, S.F., Lind, J., et al., 2015. A rotational and axial motion system load frame insert for in situ high energy x-ray studies. Rev. Sci. Instrum. 86 (9), 093902.
- Sidky, E.Y., Pan, X., 2008. Image reconstruction in circular cone-beam computed tomography by constrained, total-variation minimization. Phys. Med. Biol. 53 (17), 4777.
- Sorelli, L., Constantinides, G., Ulm, F.-J., Toutlemonde, F., 2008. The nano-mechanical signature of ultra high performance concrete by statistical nanoindentation techniques. Cem. Concr. Res. 38 (12), 1447–1456.
- Stamati, O., Andò, E., Roubin, E., Cailletaud, R., Wiebicke, M., Pinzon, G., Cyrille, C., Hurley, R., Caulk, R., Caillerie, D., et al., 2020. Spam: software for practical analysis of materials. J. Open Source Softw. 5 (51), 2286.
- Stamati, O., Roubin, E., Andò, E., Malecot, Y., 2018. Phase segmentation of concrete x-ray tomographic images at meso-scale: Validation with neutron tomography. Cem. Concr. Compos. 88, 8–16.
- Stamati, O., Roubin, E., Andò, E., Malecot, Y., 2019. Tensile failure of micro-concrete: from mechanical tests to FE meso-model with the help of X-ray tomography. Meccanica 54 (4), 707–722.
- Sun, Z., Garboczi, E.J., Shah, S.P., 2007. Modeling the elastic properties of concrete composites: Experiment, differential effective medium theory, and numerical simulation. Cem. Concr. Compos. 29 (1), 22–38.
- Sutton, M.A., Orteu, J.J., Schreier, H., 2009. Image Correlation for Shape, Motion and Deformation Measurements: Basic Concepts, Theory and Applications. Springer Science & Business Media.
- Tanaka, K., 1972. Note on volume integrals of the elastic field around an ellipsoidal inclusion. J. Elast. 2, 199–200.
- Thakur, M.M., Henningsson, N.A., Engqvist, J., Autran, P.-O., Wright, J.P., Hurley, R.C., 2023. On mesoscale modeling of concrete: Role of heterogeneities on local stresses, strains, and representative volume element. Cem. Concr. Res. 163, 107031.
- Torquato, S., Haslach, Jr., H., 2002. Random heterogeneous materials: microstructure and macroscopic properties. Appl. Mech. Rev. 55 (4), B62–B63.
- Ulm, F.-J., Constantinides, G., Heukamp, F.H., 2004. Is concrete a poromechanics materials?—A multiscale investigation of poroelastic properties. Mater. Struct. 37 (1), 43–58.
- Wei, D., Hurley, R.C., Poh, L.H., Dias-da Costa, D., Gan, Y., 2020. The role of particle morphology on concrete fracture behaviour: A meso-scale modelling approach. Cem. Concr. Res. 134, 106096.
- Yang, C.-C., Huang, R., 1996a. Double inclusion model for approximate elastic moduli of concrete material. Cem. Concr. Res. 26 (1), 83–91.
- Yang, C.-C., Huang, R., 1996b. A two-phase model for predicting the compressive strength of concrete. Cem. Concr. Res. 26 (10), 1567–1577.
- Zaoui, A., 2002. Continuum micromechanics: survey. J. Eng. Mech. 128 (8), 808–816.
 Zhai, C., Herbold, E.B., Hurley, R.C., 2020. The influence of packing structure and interparticle forces on ultrasound transmission in granular media. Proc. Natl. Acad. Sci. 117 (28), 16234–16242.